Gamma decay of pygmy states from inelastic scattering of ions

A. Bracco[1,2,a], F.C.L. Crespi[1,2], and E.G. Lanza[3]

[1] Dipartimento di Fisica dell'Università degli Studi di Milano, I-20133 Milano, Italy
[2] INFN, Sezione di Milano, I-20133 Milano, Italy
[3] INFN, Sezione di Catania, I-95123 Catania, Italy

Abstract. An overview of relevant results on the study of 1^- states focusing on their excitation with nuclear probes is given. Results obtained for the ^{90}Zr, ^{124}Sn, and ^{208}Pb nuclei using the $(^{17}\mathrm{O}, ^{17}\mathrm{O}'\gamma)$ reaction are compared with available data obtained with the (γ, γ'), $(\mathrm{p}, \mathrm{p}')$, and $(\alpha, \alpha'\gamma)$ reactions. These comparisons allow to learn on the nature of the populated states, particularly the E1 states, whose isospin character is presently poorly known. The DWBA description of the data is discussed in terms of different form factors, standard collective form factor and form factors obtained by folding microscopically calculated transition densities. The relevant aspects related to the used theoretical approach are also presented. The main objective of the analyses is the extraction of the values of the fraction of the energy weighted sum rule strength for the isoscalar dipole excitation. For completeness, in all cases, the DWBA analysis was made also for the excitations of 2^+ and 3^- states.

1 Introduction

A powerful method to study the properties of a physical system is to subject it to external perturbations and examine its response. For the atomic nucleus subjected to the absorption of photons, the response of electric dipole type is characterized in the energy region between 10 and 30 MeV by a broad bump, the Isovector Giant Dipole Resonance (IVGDR). This resonance corresponds to a dipole-type oscillation of protons against neutrons and its spectral distribution is in general well described by a Lorentzian function. Although the general properties of the IVGDR have been extensively studied during the years, there is presently particular attention to the electric dipole response in the region around the particle binding energy (< 10 MeV). In that region an additional concentration of E1 strength exceeding the Lorentzian shape was identified in many nuclei, particularly the neutron-rich ones. This E1 strength is denoted as Pygmy Dipole Resonance (PDR) and within the hydro dynamical model is described as due to oscillations of neutrons forming a skin outside a core made out of the other neutrons and protons occupying the same nuclear orbitals. Since 1969, year in which the notation pygmy strength started to be used and its influence on neutron capture was established, many experimental and theoretical works were made (see [1]). Very detailed investigations have been carried out in different mass regions for several stable nuclei and for few nuclei far from the stability valley by using radioactive beams. In the case of light nuclei, as for example for the exotic ^{11}Li nucleus [2], the pygmy, or E1 soft excitation, is characterized by a strength which does not have a resonant character and it is solely related to the single-particle structure of the loosely bound nucleons. For heavier nuclei, experimental information on pygmy states comes from experiments using real and virtual photons. Virtual photons from Coulomb excitation processes at high bombarding energy were exploited for the radioactive beams ^{132}Sn [3], ^{68}Ni [4,5] and ^{26}Ne [6]. In the case of stable nuclei experiments using virtual photons from polarized protons at 295 MeV (see, *e.g.*, [7]) were made at RNCP and several real photon scattering experiments (γ, γ') were performed for many nuclei (see [8] for a review).

Investigations employing $(\alpha, \alpha'\gamma)$ and $(^{17}\mathrm{O}, ^{17}\mathrm{O}'\gamma)$ reactions were also made. In contrast with the photon probe, for which the long-range electromagnetic field is sampling the nucleus as a whole, nuclear probes with their short-range interactions are sampling mainly the nuclear surface when their bombarding energy is less than approximately 100 MeV/u. These will be discussed in particular in this paper.

There are two important physical aspects related with the position and strength of the PDR in nuclei. One is its influence on reaction rates in the astrophysical r-process [9–11] which synthesizes approximately 50% of the abundance of the elements heavier that iron. Indeed the low-lying strength affects the synthesis of nuclei in explosive stellar burning phases, the photo-disintegration of

[a] e-mail: Angela.Bracco@mi.infn.it

ultra-high-energy cosmic rays and may be important for generating neutrons in stars. The relevant energy window for (γ, n) reactions in the stellar photon bath is located in the vicinity of the PDR. Extrapolations of the E1 response to exotic systems based on reliable data and model descriptions of nuclei in the valley of stability are needed.

The other physical aspect is the link of pygmy states to the equation of state of neutron-rich matter [12, 13] and also to corresponding objects in the universe such as neutron stars [14]. More details on this are in sect. 2.

A key question concerning pygmy states is the understanding of their nature and for that one needs to excite them not only with the Coulomb field but also using the nuclear interaction. This paper will mainly focus on the problem of finding evidence that neutrons in nucleus skins play a major role in the structure of pygmy states. The isospin character of pygmy states will be discussed in this paper and this discussion is based on recent experimental and theoretical results.

2 The neutron skin and the dipole response

In neutron-rich nuclei, because of the saturation of the nuclear density, excess neutrons are expected to form a skin and the motion of this skin originates the pygmy resonance in the E1 response. Several theoretical works (see [14–21]) suggest that the strength of the pygmy states and in particular the nuclear dipole polarizability are related to the size of the neutron skin. The neutron skin of neutron-rich nuclei is directly related to the equation of state (EOS) of asymmetric matter close to saturation density. The density dependence of the symmetry energy governs the neutron skin in nuclei as well as the radius of neutron stars [14]. Huge theoretical and experimental efforts have been devoted in recent years to constrain the isospin asymmetric part of the EOS, *i.e.*, the symmetry energy, and its density dependence (see, *e.g.*, refs. [12, 13] and [22]). The electric dipole (E1) response of nuclei and, in particular, its dependence on the neutron-to-proton asymmetry, is governed by the symmetry energy and its density dependence. The Pygmy Dipole Resonance (PDR) [1], has been utilized in several works to constrain the symmetry energy or the neutron-skin thickness. It has been also pointed out in ref. [15] that the electric dipole polarizability α_D of the nucleus provides a more robust and less model-dependent observable to extract the neutron skin thickness Δr_{np}. The dipole polarizability, which is indeed very sensitive to low-lying E1 strength due to its inverse energy weighting, is defined as

$$\alpha_D = \frac{\hbar c}{2\pi^2} \int_0^\infty \frac{\sigma(E)}{E^2} \mathrm{d}E, \qquad (1)$$

where $\sigma(E)$ is the photo-absorption cross section. Up to now there are only three measurements of the dipole polarizability: on ^{208}Pb, ^{120}Sn and on ^{68}Ni. In fig. 1 the polarizability measured for ^{68}Ni (from [5]) is shown in comparison with model predictions. Table 1 reports the values of the neutron skin obtained from the analysis of the pygmy states and from the dipole polarizability. The mild model dependence of the approach used to extract

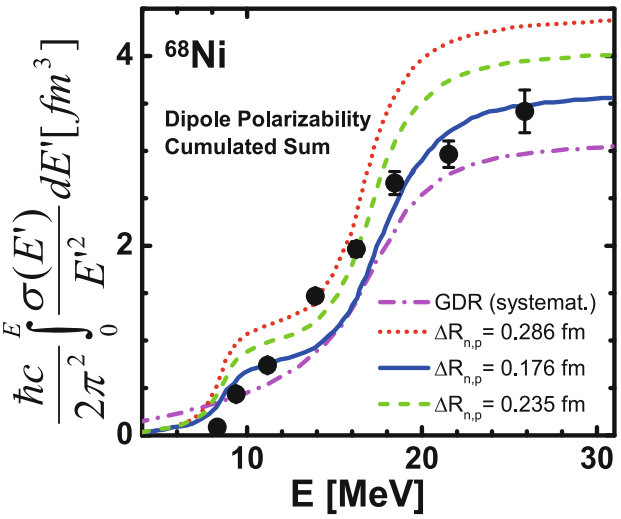

Fig. 1. (Color online) Experimental dipole polarizability cumulated sum with corresponding FSUGold calculations. The curve for the GDR from systematics is shown as well for comparison (see legend). Adapted from [5].

Table 1. Dipole polarizability, strength of the pygmy states and the deduced neutron skin radii.

Nucleus	α_D ($\mathrm{fm}^3/\mathrm{e}^2$)	PDR (% of EWSR)	Δr_{np} (fm)	Ref.
^{68}Ni	–	5(1.5)	0.200(15)	[20]
^{68}Ni	3.40(23)	–	0.17(2)	[5]
^{120}Sn	8.93(36)	–	0.148(34)	[23]
^{132}Sn	–	4(3)	0.258(24)	[20]
^{208}Pb	20.1(6)	–	$0.156^{+0.025}_{-0.021}$	[7]

the neutron skin radius was found to be further reduced by correlating the product of α_D and the nuclear symmetry energy at saturation density J with Δr_{np} yielding a value of $\Delta r_{np} = 0.165\,\mathrm{fm}$ for ^{208}Pb. These results for the neutron skin radii are connected to values of the derivative of the symmetry energy and the latter has been also obtained from complex analyses of multifragmentation reactions at density lower than saturation and from antiprotonic atoms ([24]). In addition, a recent work on π_0 photoproduction allowed to deduce the neutron skin thickness in ^{208}Pb ($\Delta r_{np} = 0.15 \pm 0.03\,\mathrm{fm}$, see [25]). The important point which is relevant in connection with the pygmy states and the nuclear polarizability is that the values of the neutron skin derived from the measurements are model dependent. It is therefore very important to give additional experimental constraints to theory. In order to understand better the nature of the pygmy states one has to obtain information also on wave functions and transition densities. The measurements aiming at providing such information are discussed in this paper in the next sections.

3 Theoretical approach

The systematics and details of the low-lying E1 strength are a matter of ongoing discussions. There are various

ways to create a dynamic electric dipole moment in a nucleus. The best way to describe the structure of a heavy nucleus is achieved by microscopic self-consistent mean field models which are based either on the Skyrme and Gogny non-relativistic interaction or on the relativis-tic meson-exchange Lagrangians. Many of these theoret-ical approaches have been used for the description of the low-lying dipole states (see ref. [26] and references therein). For spherical and closed shell nuclei the use of the Hartree-Fock (HF) plus Random Phase Approxima-tion (RPA) is the most appropriate tool for the descrip-tion of the internal structure [20, 27–33]. For open shell and deformed nuclei the use of Hartree-Fock-Bogoliubov plus Quasi-Particle RPA is employed for the description of the PDR [34–38]. Extensions of these particle-hole ap-proaches taking into account two-particle two-hole contri-butions, like the second RPA approach [39, 40], as well as the coupling to two- or three-phonon configurations have also been extensively used in the description of the low-lying dipole states. Among the latter one can quote the Extended Theory of Finite Systems (ETFFS) [41] or the Quasi-particle Phonon Model (QPM), which takes into account explicitly the coupling between nucleons and phonons [19, 42]. Relativistic mean-field theory, like RRPA [16, 17, 21, 43, 44] or the RQRPA [45–47], based on finite meson exchange representation give a good de-scription of the properties of nuclei along the stability valley as well as for the exotic nuclei. A good descrip-tion of the PDR features is obtained also within the Relativistic Quasi-particle Time Blocking Approximation (RQTBA) [11,48,49] where the quasi-particle-phonon cou-pling is taken into account.

All these calculations coincide on the main characteristic of these states, namely the presence of a strong mixing of isoscalar and isovector character. However, they differ on some other properties like their possible collective nature which is still now under debate. They coincide also on the fact that the PDR is originated in nuclei with $N/Z > 1$ by the excitation of the neutron excess. Therefore, their strengths are more intense in the exotic nuclei with neutron skin but they are also present in neutron-rich stable nuclei. As an example, we show in fig. 2 the predicted dipole response to an isovector (panel (a)) and isoscalar (panel (b)) probe for the ^{90}Zr nucleus. The strengths were produced by performing a discrete HF plus RPA calculation with a SGII interaction [29,30], the curves are generated by a smoothing procedure using a Lorentzian with a 1 MeV width. In panel (a) of fig. 2 the isovector response generated by the isovector dipole operator is shown. This operator is given by

$$O_{1M}^{(IV)} = 2\frac{Z}{A}\sum_{n=1}^{N} r_n Y_{1M}(\hat{r}_n) - 2\frac{N}{A}\sum_{p=1}^{Z} r_p Y_{1M}(\hat{r}_p). \quad (2)$$

On the other hand, a $3\hbar\omega$ dipole nuclear transition is possible and is generated by the second order dipole transition operator

$$O_{1M}^{(IS)} = \sum_{i=1}^{A}\left(r_1^3 - \frac{5}{3}\langle r^2\rangle r_i\right) Y_{1M}(\hat{r}_i). \quad (3)$$

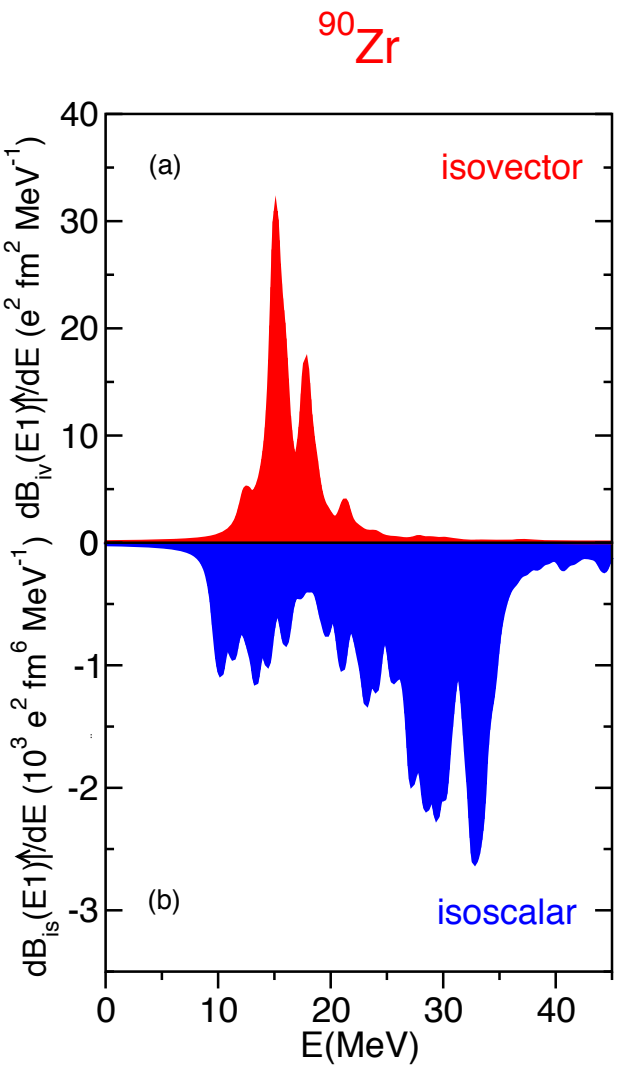

Fig. 2. (Color online) RPA strength distributions for isovector (a) and isoscalar (b) response for ^{90}Zr.

The isoscalar response is plotted in panel (b) of fig. 2. The two figures are dominated by the very well known peaks of the IVGDR, at around 15 MeV, in the upper frame and the ISGDR at 30 MeV in the lower one. In the upper panel, the peak at about 12 MeV corresponds to the PDR and we note that there is also a prominent peak in the isoscalar strength. These three different peaks at different excitation energies correspond to different excitation modes as can be evidenced by the different structure of their transition densities. In fig. 3 we plot the proton (black dash line), neutron (red, dot-dashed line), isoscalar (blue solid line) and isovector (green solid line) transition densities for the three states of interest. In the middle panel one sees the typical behavior of the isovector GDR with the proton and neutron transition densities out of phase giving rise a strong isovector transition density. This corresponds to the macroscopic picture of the GDR produced by an oscillation of protons against neutrons. The curves shown in panel (c) of fig. 3 indicate that proton and neutron transition densities are in phase in the interior and that

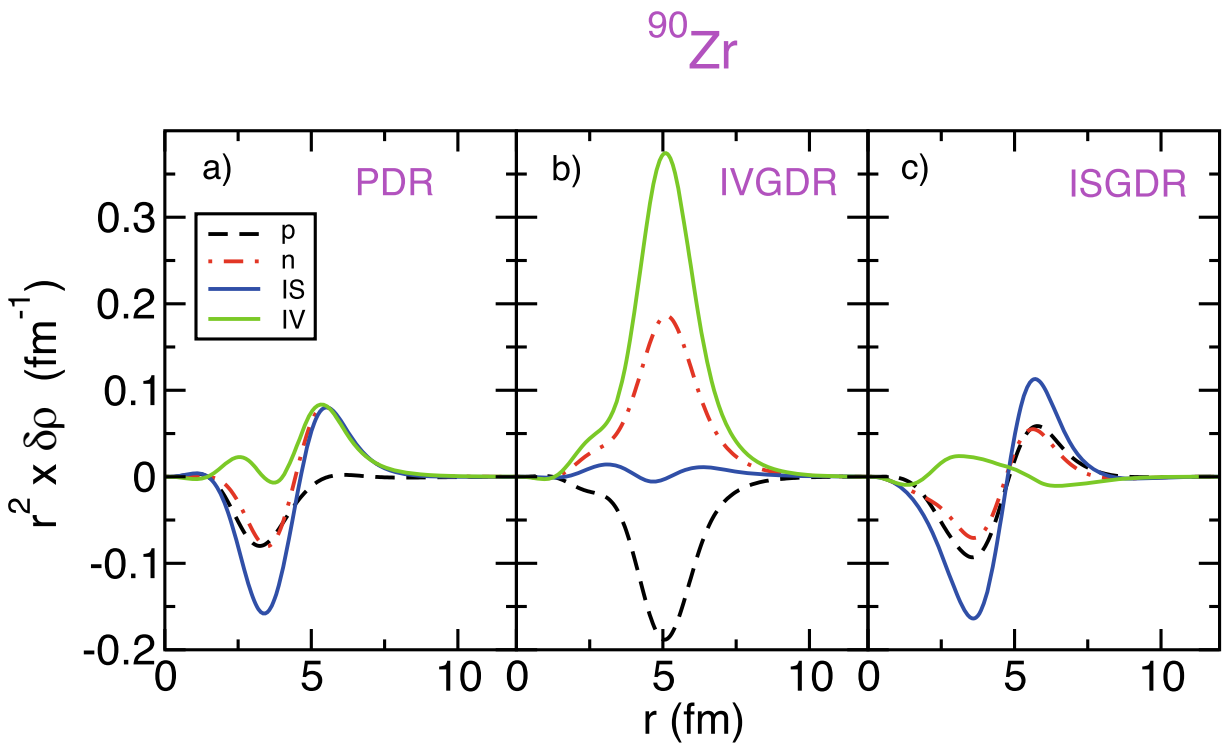

Fig. 3. (Color online) Transition densities for the low-lying dipole state (PDR) (a), for the IVGDR (b) and for the ISGDR (c) for the ^{90}Zr isotope. We show the proton, neutron, isoscalar and isovector components (as indicated in the legend).

on the nuclear surface there is a strong isoscalar transition density for the ISGDR with a node at the interior of the nucleus. This is a typical behavior of a compressional mode. The transition densities of panel (a) of fig. 3 show a different and novel behavior: the ones for neutrons and protons are in phase inside the nucleus and at the surface only the neutrons are contributing to the isoscalar and isovector transition densities making them of the same intensity in this external region. These features were found in all the many-body theory calculations cited above and therefore can be considered as the theoretical definition of the PDR. We note also that the tails of neutron transition densities extend themselves to a larger radius than the proton ones. This is another indication that this mode is generated by the less bound nucleons, whose wave functions have a longer tail outside the nuclear radius. Indeed, it has been shown in many microscopic calculations that these modes are built up essentially by particle hole configurations of neutron belonging to the neutron skin [29,44]. The strong mixing of isoscalar and isovector components allows the population of these states by means of both isoscalar and isovector probes.

The use of the isoscalar probes will be reviewed in sects. 4 and 5. The use of these projectiles is justified by some calculation performed within a semiclassical model which assumes that the motion of the two nuclei can be described according to the classical mechanics. This is true when the De Broglie wave length associate with the incident particle is small with respect to a characteristic distance of the process, like the distance of closest approach. In the Coulomb scattering, for instance, this condition is satisfied when the Sommerfeld parameter is much larger than one. These assumptions are known to be valid for heavy ion collisions of grazing type. Therefore, the two colliding nuclei move according to a classical trajectory determined by the Coulomb plus nuclear fields, while the inelastic excitations are described according to quantum mechanics. In this model, the Hamiltonian for the nucleus whose excitation one wants to describe is formed by two parts: one describing the internal structure of the nucleus and the other one is given by the external field responsible for the excitation of one partner of the reaction through the mean field of the other one. The time evolution of the eigenstates of the internal Hamiltonian is described by the Schrödinger equation which can be cast into a set of coupled first order differential equations for the time-dependent probability amplitude of the channels wave functions. The semiclassical coupled channel equations obtained in this way have to be solved for each impact parameter, providing the excitation probability for each of the states we take into account. Then, the excitation cross section for each of these states is obtained by an integration of the excitation probabilities of the states over the interval of the impact parameters contributing to the reaction. In ref. [29,30] more details are given. The states considered in the excitation process are usually determined by a mean field model like the HF plus RPA as quoted above. In the case there are many states with significant Energy-Weighted Sum Rule (EWSR) belonging to the same energy region, one bunches them together by taking as energy their average energy with the condition that the EWSR must be preserved.

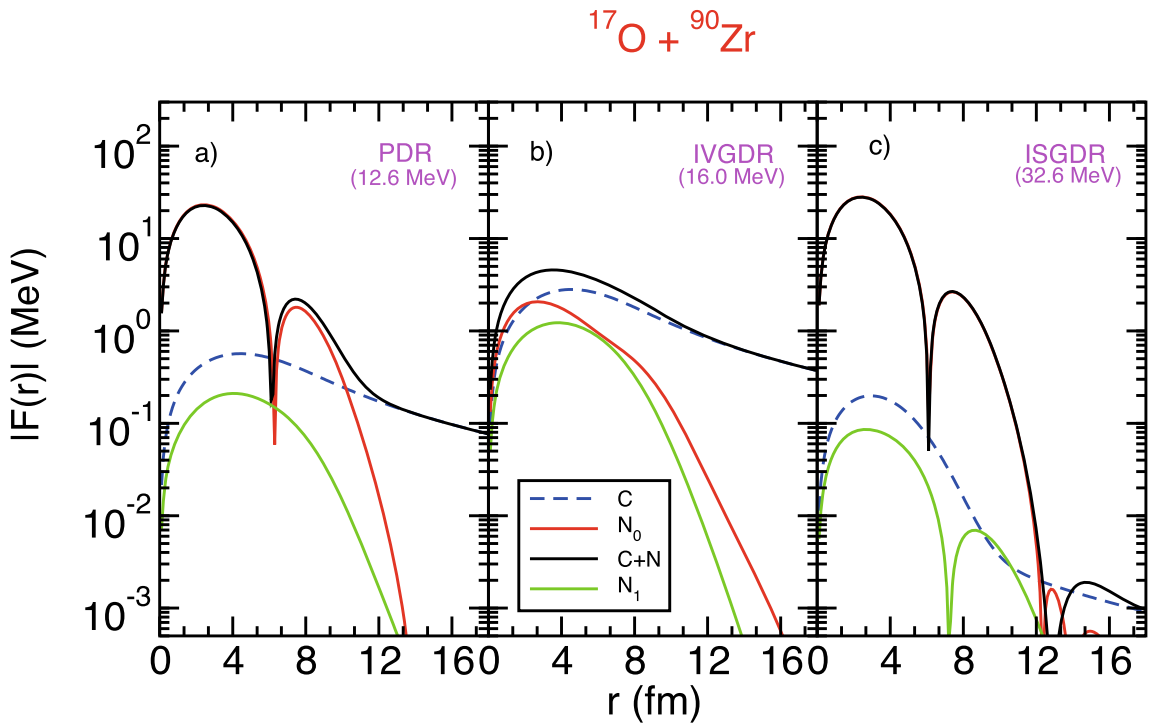

Fig. 4. (Color online) Form factors for the system $^{17}\mathrm{O} + ^{90}\mathrm{Zr}$ for the PDR state (panel (a)), the isovector GDR (panel (b)) and for the ISGDR (panel (c)). In each frame there are reported the nuclear and Coulomb (blue dashed line) contributions, as well as the total one (black solid line). For the nuclear part we have the two contributions: isoscalar (red solid line) and isovector (green solid line); in the legend they are indicated as N_0 and N_1, respectively.

The classical trajectory along which the nuclei move during the reaction is determined by the Coulomb interaction and by the real part of the optical potential which is constructed within a double-folding procedure [50]. This consists in considering a nucleon-nucleon interaction between two particles, each of them belonging to one of the two reaction partners; the contribution of all the other nucleons is obtained by integrating the product of the nucleon-nucleon interaction with the densities of the two nuclei, over the internal radii of the two ions. If one takes into account also the isospin-dependent part of the nucleon-nucleon interaction then the folding potential will be formed by two parts, one depending of the central part of the interaction and the other one depending of the isospin degree of freedom. This latter part will go to zero when one of the two reaction partners has $N = Z$ [51]. The form factors are also obtained within the double-folding procedure where one of the densities is replaced by the transition density of the state one wants to study. Again, if one takes in consideration the isospin-dependent part of the nucleon-nucleon interaction then two components are obtained for the nuclear form factors:

$$F_0 = \iint \left[\delta\rho_n^A(r_1) + \delta\rho_p^A(r_1)\right] \times v_0(r_{12})\left[\rho_p^B(r_2) + \rho_n^B(r_2)\right] r_1^2 \mathrm{d}r_1 r_2^2 \mathrm{d}r_2 \quad (4)$$

$$F_1 = \iint \left[\delta\rho_n^A(r_1) - \delta\rho_p^A(r_1)\right] \times v_1(r_{12})\left[\rho_n^B(r_2) - \rho_p^B(r_2)\right] r_1^2 \mathrm{d}r_1 r_2^2 \mathrm{d}r_2, \quad (5)$$

where the $\delta\rho_i$ $(i = n, p)$ are the transition densities of the state of the nucleus A under study which is excited by the mean field of nucleus B. In previous works [29,30] and also in the calculation presented here, for the isoscalar and isovector components of the nucleon-nucleon interaction (v_0 and v_1) use was made of the Reid-type version of the M3Y nucleon-nucleon interaction [50,52] which is not density dependent. Few differences, but only in the interior part of the nucleus, are reported among the ion ion potentials obtained when the density dependence is taken into account while at the surface the potential are almost identical [53, 54]. Therefore, since the reactions studied with this model explore the peripheral region of the two colliding nuclei, the use of the M3Y interaction, as employed here, seems to be well justified.

The radial form factors for the system $^{17}\mathrm{O} + ^{90}\mathrm{Zr}$ and for the three representative states illustrated above are shown in fig. 4. The various contributions as they are shown in the legend, are plotted separately. For the nuclear part the two contributions discussed above are plotted (eqs. (4) and (5)). Note that the one depending on the isospin gives a very small contribution to the PDR and ISGDR. Indeed, this contribution is two orders of magnitude smaller than the central term part. This feature, together with the fact that we use the $^{17}\mathrm{O}$ projectile at an incident energy of 20 MeV/u, allows to consider $^{17}\mathrm{O}$ as an effective isoscalar probe (see discussion below). Due to its isoscalar nature, the ISGDR has a strong nuclear form factor and almost an insignificant Coulomb one. Conversely, for the isovector GDR state one has the opposite behavior: the

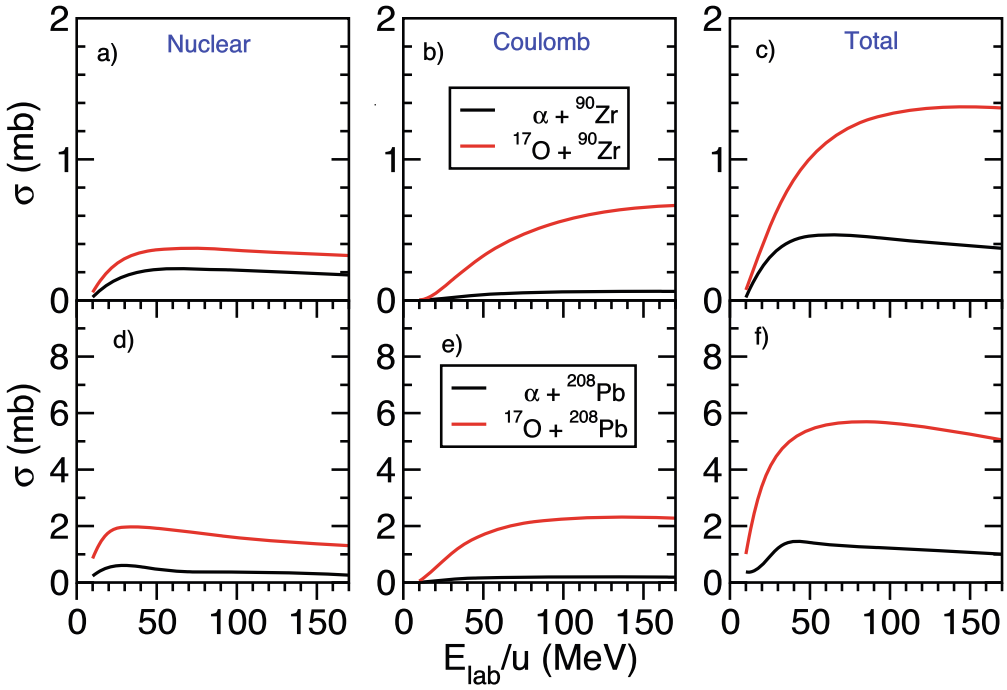

Fig. 5. (Color online) Inelastic cross sections for the PDR state as function of the incident energy per nucleon for the two systems, $\alpha + {}^{90}$Zr and ${}^{17}\mathrm{O} + {}^{90}$Zr. The nuclear (a) and Coulomb (b) contributions, as well as the total one (c), are shown in separate frames (a), (b) and (c), respectively. In the lower frames the inelastic cross sections for $\alpha + {}^{208}$Pb and ${}^{17}\mathrm{O} + {}^{208}$Pb are shown.

Coulomb form factor is the dominant one. However, for nuclei where the ratio N/Z is larger the contribution of the nuclear part becomes more important. The N_0 component of the IVGDR form factor has a different shape in comparison with the other two, namely no oscillation pattern. This is due to the fact that for this state the isoscalar transition density, which enters in the calculation of this form factor, is almost flat with very little oscillations (see fig. 3(b)). For the PDR we have a negative interference (not appreciable in the figure), between the Coulomb and the nuclear contribution, at small radii and a positive one at the peripheral region which is due to the node of the isoscalar transition density at the interior of the nucleus [29]. Since we are dealing with reactions involving the surface of nuclei, such positive interference will have an effect also on the inelastic cross sections. The last thing to stress concerns the different slope of the peripheral part of the nuclear form factor. In the present case this is not evident at a simple glance at fig. 4, but if one superimposes the nuclear form factor for the PDR state to the other ones it is possible to clearly appreciate that the former has a different slope and it extends to a larger distance. Again, the main difference is around the nuclear radius and therefore these differences will have consequences on some quantities related to grazing reaction processes, like the differential cross section. This is pointed out in the next sections in connection with the comparison of predictions using microscopic and macroscopic form factors with the experimental results. There, we shall clearly show that the use of standard form factors for the PDR, constructed with transition densities like the Goldhaber-Teller or Tassie ones as well as the ones deduced for the ISGDR [55, 56] (which assume that the states are pure isovector) fails to describe the data. It is evident the need of using predictions obtained with form factors deduced from microscopic transition densities which incorporate the main features of these states, namely the strong mixing of isoscalar and isovector characters. The use of a proper form factor in the study of the PDR is of paramount importance in order to determine the correct values for some relevant quantities characterizing these new modes [57].

In order to illustrate the behavior of the two isoscalar probes used until now, we have performed calculations for inelastic scattering cross sections within the semiclassical model described above for the two systems $\alpha + {}^{90}$Zr and ${}^{17}\mathrm{O} + {}^{90}$Zr. We are aware of the fact that the use of a semiclassical model introduces some uncertainties in the calculations. In particular we are thinking of the absence of interference among the classical trajectories which guarantees that only the total cross section can be considered as a reliable result. A further uncertainty may be due to the imaginary part of the optical potential for the cases where an indirect knowledge, through the elastic scattering measurement, is missing. In such a case a standard assumption is made by taking as imaginary part a potential with the same geometry of the real part and half intensity. The following calculations have been performed by such choice because we want to show the general characteristics of these excitation processes. However, the calculations in sect. 5, done to interpret the experimental data, were performed using the optical potential extracted from the elastic scattering measurement. The results are shown in the top panels of fig. 5, where the inelastic cross sec-

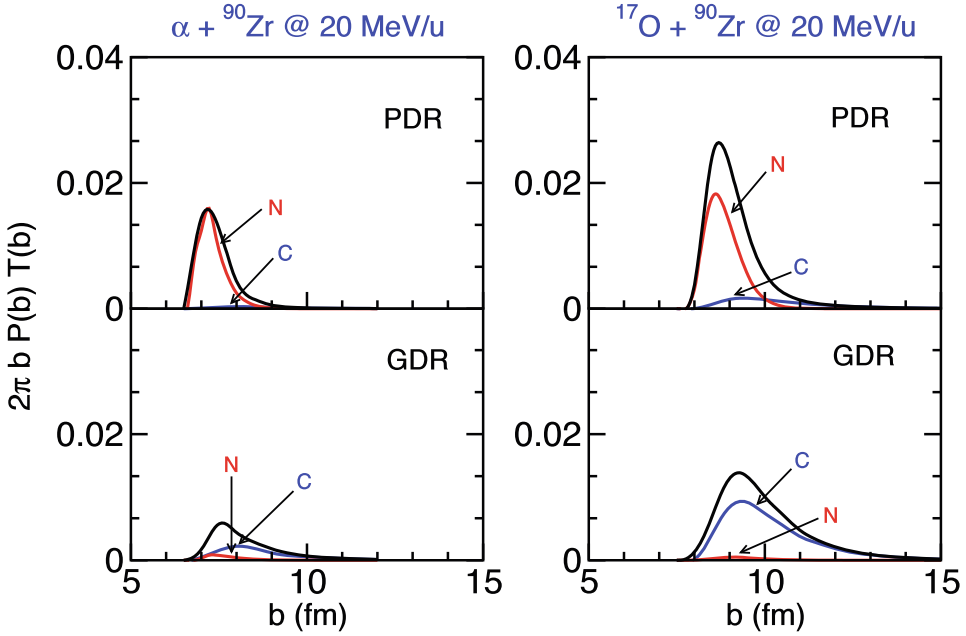

Fig. 6. (Color online) Partial wave cross sections as a function of the impact parameter b for the system $\alpha+{}^{90}$Zr and ${}^{17}\mathrm{O}+{}^{90}$Zr at 20 MeV/nucleon. In each column are reported the results for the two dipole states, PDR (upper frame) and GDR (lower frame). In each graph the Coulomb and nuclear contributions are reported and explicitly indicated. The black curve is obtained when both contribution are taken into account.

tions are plotted as a function of the incident energy per nucleon. The excitation induced by the nuclear and by the Coulomb interaction are reported in panels (a) and (b), respectively. The result obtained when both interactions are taken into account is plotted in panel (c). As it is well known, the α projectile is an almost pure isoscalar probe, being the Coulomb excitation almost zero in the entire incident energy interval considered here. In addition, the ^{17}O projectile can be considered as a very good isoscalar probe at bombarding energy around 20 MeV/u. Indeed, at these energies, the Coulomb excitation is very low, while the nuclear interaction is rapidly increasing. Therefore, at incident energies around 20 MeV/u, while the Coulomb excitation for the two probes is almost zero, the cross section due to the nuclear interaction is almost double for the ^{17}O projectile, with respect to the α projectile. At higher energies, for both probes a strong positive interference between the Coulomb and nuclear contributions is manifestly evident, even for the very small contribution of the Coulomb interaction in the α projectile case. Inelastic scattering cross sections for the two systems, $\alpha+{}^{208}$Pb and ${}^{17}\mathrm{O}+{}^{208}$Pb, are shown in the bottom panels of fig. 5. The figure shows the same pattern as the two previous cases, the difference being only in the magnitude of the inelastic cross section.

In the semiclassical model the differential angular distribution is associated to different ranges of impact parameters. In fig. 6 we reported a quantity, which can be thought of as a partial-wave cross section, as a function of impact parameter. This quantity integrated along the impact parameter range, gives the total excitation cross section for the state under consideration. The integrand is composed by the probability $P(b)$ of exciting the considered state, which depends on the impact parameter b. Such probability is modulated by the transmission coefficient $T(b)$ which includes processes which are not taken explicitly into account. A standard way to construct it is from an integral along the classicl trajectory of the imaginary part of the optical potential which governs the elastic scattering of the studied reaction. For more details see ref. [29]. In fig. 6 the partial wave cross section is reported for the two reactions, $\alpha+{}^{90}$Zr and ${}^{17}\mathrm{O}+{}^{90}$Zr, at 20 MeV/$u$ for the two dipole states PDR and IVGDR. In each frame the Coulomb (blue line) and nuclear (red line) contributions are explicitly shown as well as the total one (black line). In the two cases, and for this incident energy, the Coulomb contribution, for the PDR state, is very small in comparison to the nuclear one. For the IVGDR, it occurs the other way around. Nuclear excitations are enhanced at grazing angles, that is they get contributions from a limited range of impact parameters, while for the Coulomb interaction a larger range of impact parameter give their contribution.

The positive interference appears clearly in the differential cross section which is usually used to extract the magnitude of useful significant physical quantities like the reduced transition probability B(EL). As an example, we show in fig. 7 the differential cross section for the system $\alpha+{}^{90}$Zr for two incident energies, 20 and 35 MeV/u. The calculations were made with the code DWUCK4 [58] using the microscopic form factors and the double-folding potentials described above. The imaginary part was chosen to have the same geometry as the real part and with half strength. The contribution due to only the nuclear interaction is plotted separately (red solid line) in order to show evidence of the interference effect with the, although very small, Coulomb contribution. The maximum differ-

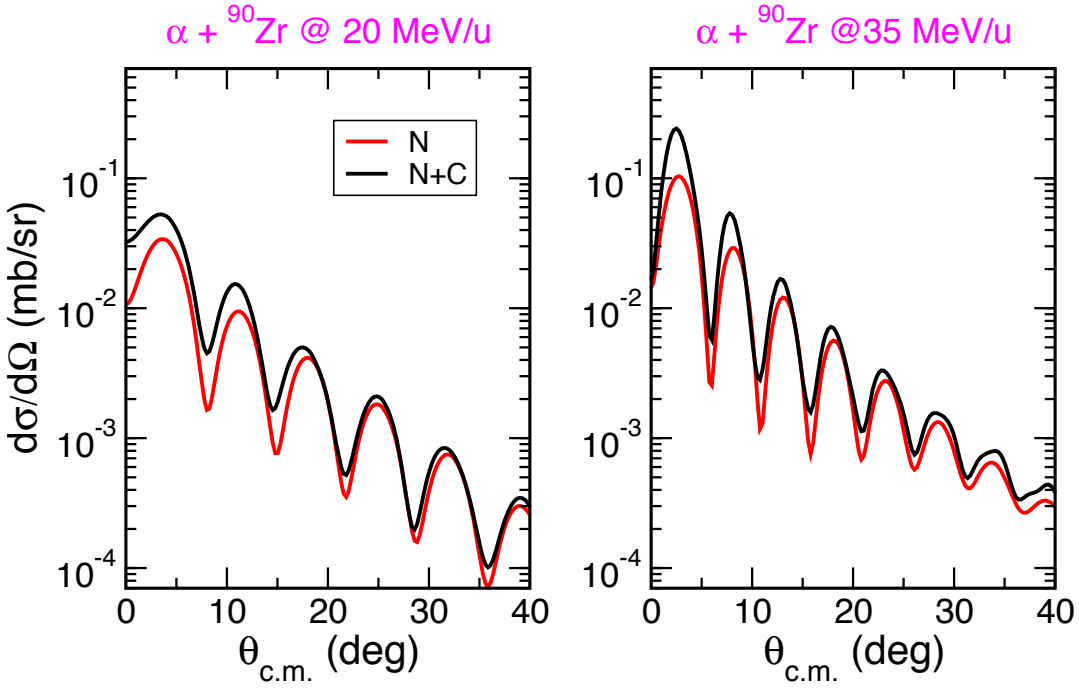

Fig. 7. (Color online) Differential cross sections for the PDR state as a function of the center-of-mass angles for the system $\alpha + {}^{90}$Zr at two different incident energies. The nuclear (red line) and nuclear plus Coulomb (black line) cross sections are separately shown. The positive interference effect is more evident for the 35 MeV/u incident energy case (right panel).

ence between Coulomb and Coulomb plus nuclear differential cross sections is found to be approximately a factor of two for the 35 MeV/u case, and is located at very forward angles, that is, around the grazing region where the positive interference is larger. At larger angles the two curves are not very different from each other. In the case of the $({}^{17}\mathrm{O}, {}^{17}\mathrm{O}'\gamma)$ reaction, comparisons between the experimental differential cross sections and theoretical calculations, based on microscopic form-factors, are shown and discussed in sect. 5.

4 The pygmy states populated via inelastic scattering of alpha particles

As previously discussed in the case of the dipole vibration, both isovector and isoscalar types exist in nuclei. While in the isovector oscillation, protons and neutrons move out of phase, the isoscalar strength of dipole type, the Isoscalar Giant Dipole Resonance (ISGDR), is due to a squeezing mode in the nucleus. The ISGDR at excitation energy of 20–25 MeV has been identified in several nuclei via inelastic scattering of alpha particles. For nuclear structure studies with the alpha probe there are two main characteristics that could selectively populate dipole states of isoscalar type. The first is the isospin character, namely alpha particle are predominantly isoscalar probes at energy below 150–200 MeV because Coulomb excitation hardly plays a role in the excitation of these state. The second is the sensitivity to the radial transition density on the nuclear surface.

Consequently, if one wants to learn about the underlying structure of pygmy states and about their isospin character it is important to compare the excitation cross section of these states with isovector probes (as photons) and isoscalar probes as, for example, alpha particles or heavier ions as C and O below 30 MeV/u. The pioneering work of Poelhekken *et al.* [59] has demonstrated that several 1^- states are well populated using the reaction $(\alpha, \alpha'\gamma)$ and paved the way to experiments employing detector systems for gamma-ray measurements with energy resolution better than that of the NaI scintillators used in that experiment. The high resolution is particularly important in nuclei with high density of states. As an example of high density of states, the case of ^{124}Sn is shown in fig. 8, where high-resolution data from $(\alpha, \alpha'\gamma)$ and (γ, γ) are plotted.

In the last decade, the 1^- discrete states were studied in a number of nuclei with the $(\alpha, \alpha'\gamma)$ reaction at 136 MeV. In these studies the measured cross sections were compared with the B(E1) obtained from (γ, γ') measurements. Figure 9 summarizes a number of results obtained on the population of pygmy states and table 2 gives relevant information of these measurements. In fig. 9 the experimental data have been integrated in the energy intervals reported in the panels in order to have a global comparison between the two different sets of data. The comparison between these two different physical quantities is supported by the results of ref. [68]. There, calculations done according to the semiclassical model described in sect. 2 have shown that the dynamical effects entering the cross section calculations do not distort too much the isoscalar B(E1) distribution. The common feature of these measurements is that only a subset of the 1^- states

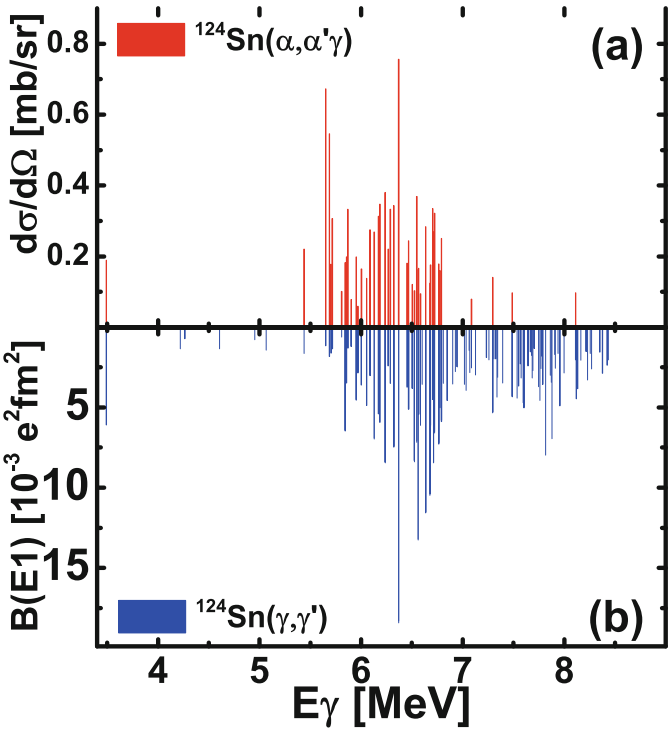

Fig. 8. (Color online) (a) Cross sections for the excitation of $J^\pi = 1^-$ in ^{124}Sn deduced from the $(\alpha, \alpha'\gamma)$ experiment. (b) The B(E1)↑ strength distribution, obtained in (γ, γ') [60]. Adapted from [61].

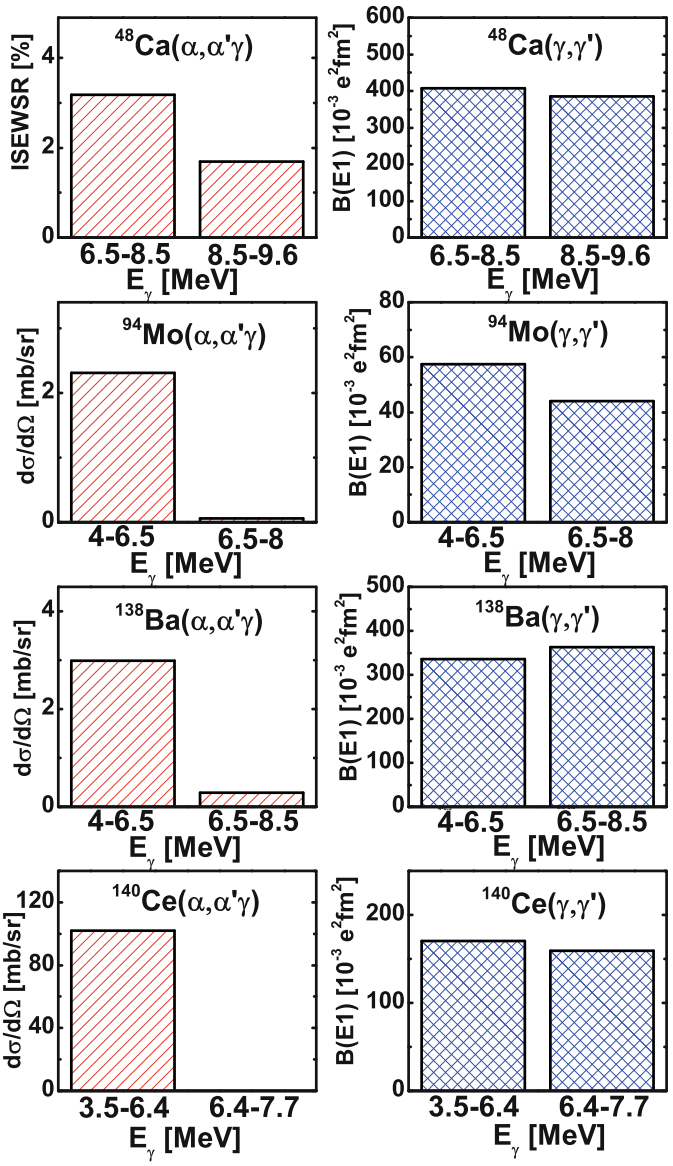

Fig. 9. (Color online) Left column: cross sections integrated in the displayed energy bins for the excitation of $J^\pi = 1^-$ in ^{48}Ca, ^{94}Mo, ^{138}Ba, ^{140}Ce deduced from the $(\alpha, \alpha'\gamma)$ experiments. Right column: the B(E1)↑ strength distribution, obtained in (γ, γ') [60].

populated via (γ, γ') is also well populated by the $(\alpha, \alpha'\gamma)$ reaction. This observation suggested that the ensemble of 1^- pygmy states consists of two different components with structurally different states. Because of the isoscalar nature of the alpha probe and because the E1 photon excitation is purely isovector, it was concluded that the lower-lying states in the PDR have a prevailing isoscalar structure, while the higher-lying states are dominantly of isovector type. It should be noted that the higher-lying dipole states could be of isovector type with or without considerable isoscalar admixture. However, there is a different interaction depth of the two probes with the nucleus. Therefore if the higher-lying states also have a large intermediate isoscalar structure with small isospin mixing but with a transition density that is peaked well inside the nuclear surface they could be populated in (γ, γ') and not in $(\alpha, \alpha'\gamma)$.

5 The pygmy states populated via inelastic scattering of ^{17}O

The existing studies for the excitation of pygmy states via the $(\alpha, \alpha'\gamma)$ reactions have shown that valuable information on the nature of the discrete 1^- states is obtained by excitation processes which involve not only the Coulomb excitation but also the nuclear part of the interaction, particularly in regimes in which the latter is dominant. Based on this finding, one expects that the use of different bombarding energies and of different types of colliding nuclei, characterized by different mixtures of isoscalar/isovector components for nuclear excitation, is very useful to reveal the characteristic features of the pygmy states. In connection to this, a number of measurements were recently done using the $(^{17}\mathrm{O}, ^{17}\mathrm{O}'\gamma)$ reaction at a bombarding energy of 20 MeV/u to investigate the structure of pygmy states [69–73]. This choice was guided by what was learned from measurements made in the eighties and nineties using this reaction but with low-energy resolution detector systems for the measurements of the gamma-rays. In fact, NaI or BaF_2 scintillators were used in those experiments and thus structures in the region of the GDR tails were not investigated. For the ^{208}Pb nucleus an experiment was done at 22 MeV/u [74] and the gamma decay from the

Table 2. Overview of experiments studying low-lying 1^- excitations using inelastic scattering of alpha particles. Adapted from [1].

Isotope	Tool	gamma det.	Comment	Ref.
^{40}Ca	$(\alpha, \alpha\gamma)$	NaI	2 states at 5.9 MeV and 6.9 MeV	[59]
^{40}Ca	$(\alpha, \alpha\gamma)$	HPGe	2 states at 5.9 MeV and 6.9 MeV	[62]
^{48}Ca	$(\alpha, \alpha\gamma)$	HPGe	6 states between 6.5 MeV and 9.8 MeV	[62]
^{58}Ni	$(\alpha, \alpha\gamma)$	NaI	6 states between 6.0 MeV and 10 MeV	[59]
^{90}Zr	$(\alpha, \alpha\gamma)$	NaI	9 states between 5.5 MeV and 9.6 MeV	[59]
^{94}Mo	$(\alpha, \alpha\gamma)$	HPGe	10 states, concentration between 4.1 MeV and 7.1 MeV	[63]
^{124}Sn	$(\alpha, \alpha\gamma)$	HPGe	45 states, concentration between 5.4 MeV and 6.8 MeV	[64]
^{138}Ba	$(\alpha, \alpha\gamma)$	HPGe	16 states, concentration between 4.5 MeV and 6.8 MeV	[65]
^{140}Ce	$(\alpha, \alpha\gamma)$	HPGe	13 states between 4.1 MeV and 6.2 MeV	[65, 66]
^{208}Pb	$(\alpha, \alpha\gamma)$	NaI	7 states between 5.3 MeV and 7.3 MeV	[59]
^{208}Pb	(α, α)	–	4 states between 4.8 MeV and 6.3 MeV	[67]

Table 3. Overview of experiments studying nuclear excitations using inelastic scattering of ^{17}O.

E_{beam}	Studied nuclei	Angles (CM)	Reaction	Studied states	Ref.
1428 MeV	^{208}Pb	1.5°–5.0°	$(^{17}\text{O}, ^{17}\text{O}')$	IVGDR, ISGQR	[76]
374 MeV	^{90}Zr, ^{208}Pb	1.5°–5.0°	$(^{17}\text{O}, ^{17}\text{O}')$	IVGDR, ISGQR	[77]
1429 MeV	^{208}Pb	1.5°–5.0°	$(^{17}\text{O}, ^{17}\text{O}'\gamma)$	IVGDR, ISGQR, ISGMR	[75]
381 MeV	^{208}Pb	13° (LAB)	$(^{17}\text{O}, ^{17}\text{O}'\gamma)$	ISGQR	[74]
375 MeV	^{204,206,208}Pb	5°–19° (LAB)	$(^{17}\text{O}, ^{17}\text{O}')$	low lying 2^+, 3^-	[78]
380 MeV	^{208}Pb	12°–22°	$(^{17}\text{O}, ^{17}\text{O}'\text{n}\gamma)$	IVGDR, ISGQR, ISGMR	[79]
340 MeV	^{208}Pb	12°–22°	$(^{17}\text{O}, ^{17}\text{O}'\gamma)$	low lying 2^+, 3^-, PDR	[70]
340 MeV	^{124}Sn	12°–22°	$(^{17}\text{O}, ^{17}\text{O}'\gamma)$	low lying 2^+, PDR	[71]
340 MeV	^{140}Ce	12°–22°	$(^{17}\text{O}, ^{17}\text{O}'\gamma)$	low lying 2^+, 3^-, PDR	[72]
340 MeV	^{90}Zr	9°–15°	$(^{17}\text{O}, ^{17}\text{O}'\gamma)$	low lying 2^+, 3^-, PDR	[73]
61 MeV	^{40}Ca	9°–60° (LAB)	$(^{17}\text{O}, ^{17}\text{O}')$	low lying	[80]
1428 MeV	^{208}Pb	1.5°–4.5°	$(^{17}\text{O}, ^{17}\text{O}'\text{n}\gamma)$	GR	[81]
1429 MeV	^{90}Zr, ^{124}Sn	1.5°–4.5°	$(^{17}\text{O}, ^{17}\text{O}'\text{n}\gamma)$	GR	[82]
1360 MeV	^{120}Sn	0°–10°	$(^{17}\text{O}, ^{17}\text{O}'\gamma)$	GDR	[83]
1429 MeV	$A = 60$–232	2.5°–6.5° (LAB)	$(^{17}\text{O}, ^{17}\text{O}')$	GR	[84]
1435 MeV	^{60}Ni, ^{90}Zr, ^{120}Sn, ^{208}Pb	1°–7°	$(^{17}\text{O}, ^{17}\text{O}')$	low lying 3^-, ISGMR, ISGQR	[85]
375 MeV	^{238}U	9°–16°	$(^{17}\text{O}, ^{17}\text{O}')$	GQR	[86]

giant quadrupole resonance (GQR) was measured while in an experiment for the same nucleus, done at 84 MeV/u, the gamma decay from the GDR [75] was measured. It is important to underline that the 84 MeV/u data show a strong Coulomb excitation of GDR while the same is not true at 22 MeV/u. In table 3 a summary of the main features of the experiments made using the $(^{17}\text{O}, ^{17}\text{O}')$ inelastic scattering to study nuclear excitations is given.

Based on these previous results and corroborated by the theoretical cross section calculations shown in sect. 2, it is clear that a bombarding energy of 20 MeV/u is ideal to excite 1^- states with an interaction mainly of nuclear type and including only a small contribution from Coulomb excitation. The ^{208}Pb, ^{124}Sn and ^{90}Zr and ^{140}Ce nuclei were studied with this reaction and the gamma decay was measured at high resolution with HPGe detectors, as in the case of the measurements discussed in the previous section for $(\alpha, \alpha'\gamma)$.

Only in the case of ^{124}Sn there are data at high resolution also from the $(\alpha, \alpha'\gamma)$ reaction (the analysis of ^{140}Ce from $(^{17}\text{O}, ^{17}\text{O}'\gamma)$ is underway), while the existing $(\alpha, \alpha'\gamma)$ measurements for ^{208}Pb and ^{90}Zr were made using NaI scintillators to detect gamma-rays and thus have low resolution. Moreover, in the case of the $(^{17}\text{O}, ^{17}\text{O}'\gamma)$ reaction data were obtained at different scattering angles and the analyses of the measured cross sections were performed within the framework of the Distorted Wave Born Approximation (DWBA). This is discussed in the next sections together with the extracted strength for the isoscalar dipole response.

5.1 Experimental technique

From the experimental point of view the use of ^{17}O is preferable as compared with the most abundant isotope ^{16}O (purer as isoscaler probe) because of its rather small binding energy (4.1 MeV). Indeed, in heavy-ion reactions, it is necessary to separate projectile and target excita-tions. In this connection the Doppler correction, needed to construct the γ-ray spectra associated to the (^{17}O, ^{17}O$'\gamma$) reaction, enables the separation of the different contribu-tions, since the velocity of the target and projectile are very different. In particular the use of ^{17}O projectiles lead to gamma-ray spectra which in the energy region > 4 MeV do not contain background from the projectile emission, usually appearing as a continuum distribution (because of the wrong Doppler correction which is made using the velocity of the target nucleus).

In contrast with light ions, for ^{17}O the pattern of the differential cross section for inelastic scattering as a function of angle does not characterize well the multipolarity of the excited states. The measurements discussed here were made at angles around the grazing angle. In particular the values of the grazing angles in the center-of-mass sys-tem are: 9.31° (^{90}Zr target), 10.72° (^{124}Sn target), 16.01° (^{208}Pb target). With heavy-ion beams, states with differ-ent multipolarity, also larger than 3, can be populated. However, the gamma decay selection rules suppress the decay to ground state for such high-spin states. An important point in this type of studies is to have measurements of the angular distribution of the emitted gamma-rays to obtain a clear identification of the spin of the populated states.

The coincidence experiments made to measure cross sections for the (^{17}O, ^{17}O$'\gamma$) reaction used a set up consisting of two main detection systems, one for the measurement of the scattered ions and one for the measurement of the gamma decay. Figure 10 shows in a schematic way the experimental setup. A system of telescopes of Si detectors was used for the identification and measurement of the kinetic energy of the scattered ions. The segmented sili-con telescopes (pixel type) were placed for each measured nucleus at around the grazing angle (see table 3) and symmetrically with respect to the beam direction. These telescopes are prototypes built for the TRACE project [87]. Each Si detector had an horizontal size of 20 mm, a ver-tical size of 50 mm and included 60 pixels each with an area of 4 mm $\times$ 4 mm. For these Si detectors *ad hoc* elec-tronic adapter boards were built which selected the 32 pixels closest to the beam direction. The front face sur-faces of the electronically connected pixels formed approx-imately a disk in the plane perpendicular to the beam at distance of 8 cm from the target center. The two ΔE-E silicon telescopes each consisted of a thin "ΔE" detector placed in front of a thick "E" detector. The ΔE detec-tors were 200 μm thick, producing an energy loss of about 70 MeV for ^{17}O ions at 340 MeV. The E detectors were 1 mm thick and this thickness was sufficient to stop the ^{17}O ions completely. The thresholds of the Si detectors were such that a large fraction of events corresponding to protons and alpha particles were rejected. The overall energy resolution (as FWHM) was typically around 0.3% at 340 MeV.

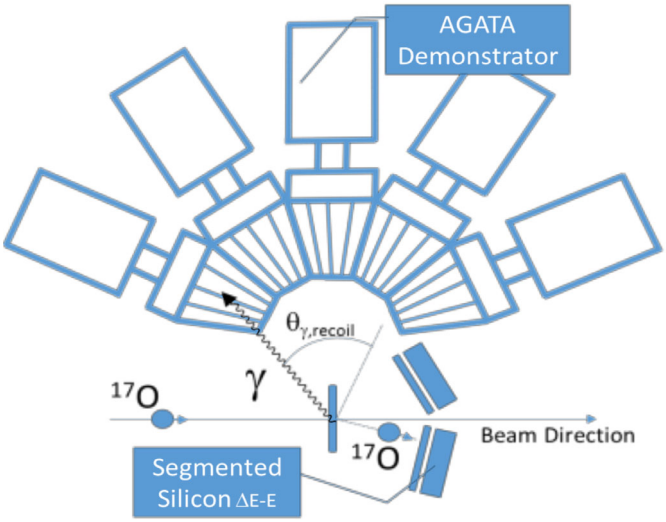

Fig. 10. Schematic representation of the experimental setup including segmented silicon detectors placed at forward angles and the AGATA HPGe detectors. The angle $\theta_{\gamma,\mathrm{recoil}}$ between the direction of the recoiling ^{208}Pb ions (dashed line) and of the gamma-ray (when a scattered ^{17}O is detected in the right silicon telescope) is displayed.

The detection of gamma-rays, emitted in coincidence with events measured in the Si telescopes, was performed with the AGATA (Advanced Gamma Tracking Array) Demonstrator. AGATA is a HPGe detector array of new generation allowing to use the techniques of pulse shape analysis and of gamma-ray tracking [88, 89]. At the time of these experiments the AGATA Demonstrator consisted of three to five triple clusters of HPGe detectors and was placed 13.5 cm from the target covering an angular range in theta from 100° to 150° (relative to the beam direction). The segmentation of the HPGe detectors allowed the direction of the gamma-ray emission to be determined with a precision of 1 degree. The AGATA detection efficiency was deduced from measurements with radioactive gamma sources and by simulations performed with the computer code GEANT4 [90, 91] including the geometrical configuration of these particular experiments.

The correlation with the beam direction was particularly useful to check with rather good precision the angular position of each pixel. For this purpose the Doppler shift of the 6.13 MeV gamma-ray transition of the ^{16}O nucleus was examined for each pixel. The ^{16}O ions were well identified from ^{17}O ions in the E-ΔE correlation of the collected events (see left panel of fig. 11). The 6.13 MeV gamma-rays coming from a source moving with the beam velocity, corresponding to a velocity parameter beta $= v/c$ of 0.2, resulted to be the most sensitive, among the available transitions, to the Doppler shift correction. This is shown in the right panel of fig. 11.

To obtain the excitation cross section for specific nuclear states data from (^{17}O, ^{17}O$'\gamma$) were used. Indeed, if

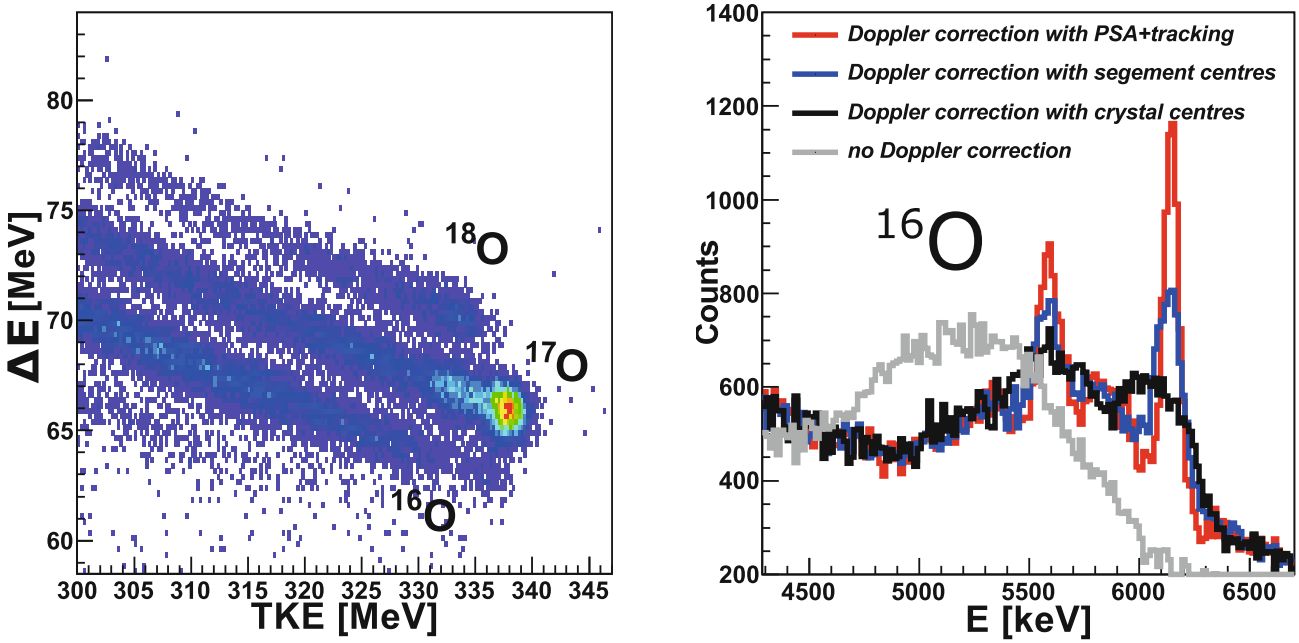

Fig. 11. (Color online) Left panel: Scatter plot of the total kinetic energy measured in one pad of the used silicon telescopes *versus* the energy deposit measured in the ΔE pad. The separation between the oxygen isotopes is shown. Right panel: Energy spectrum of the gamma-rays measured in coincidence with the $(^{17}\mathrm{O}, ^{16}\mathrm{On}\gamma)$ reaction channel. The grey spectrum is without Doppler correction, while the others were corrected using different position information as described in the legend.

one measures, in addition to the energy transferred from the projectile to the target, the gamma decay from the state with HPGe detectors the energy resolution is much improved and more states are in general identified. This requires the measurement of all the possible decay branches when the decay from an excited state does not involve only the direct decay to the ground state. In addition, since the yields were extracted from spectra for which the condition $E^* = E_\gamma$ within a window of approximately ± 1 MeV, possible feeding was evaluated by shifting the gates at higher energy. The error bars in the experimental points include all these corrections, in general rather small and mainly concerning the region below 3 MeV.

Several gamma-ray energy spectra with different conditions on the excitation energy were constructed from these types of data. The condition of gamma-ray energy equal to the nuclear excitation energy of the recoiling nucleus selects the ground state decays from the populated excited state and in the case of 1^- states the ground state decay is expected to be the dominant one. Figures 12, 13 and 14 show examples for this selection in the case of data for the ^{90}Zr, ^{208}Pb and ^{124}Sn nuclei. In all cases the ground state decay of the corresponding 1^- state can be clearly seen.

Because of the feature of the set up used for the $(^{17}\mathrm{O}, ^{17}\mathrm{O}'\gamma)$ reaction measurements it was possible to obtain for the most intense transitions an almost continuous angular distribution of the emitted gamma-rays relative to the direction of the recoiling nucleus. The direction of the recoiling nucleus was deduced from kinematics from the measured scattered particles. To give few examples the measured double differential cross section is shown in fig. 15 for three excited states in ^{208}Pb and one in ^{124}Sn. The three selected states of ^{208}Pb are the 3^- state at 2.613 MeV (top panel), the 2^+ state at 6.194 MeV (bottom panel) and the 1^- state at 5.512 MeV (middle panel) and the E1 gamma decay from the 3^- state to the first 2^+ state in ^{124}Sn. It is remarkable how the data follow very well the expected angular distribution characterising the multipolarities 1, 2, and 3 over the wide measured angular interval from 0° to 180° relative to the target recoil.

Because of the wide measured angular interval and keeping in mind that the angular pattern has a maximum at 90° for 1^- states and a minimum for 2^+ states, in the case of low intensity transitions the data were integrated over a wider angular interval. In particular, the ratio between the number of counts in the (65°–115°) and in the (15°–65°) regions was evaluated for gamma transitions in different energy regions to deduce their multipolarities. The data displayed in fig. 16, concerning the ^{208}Pb nucleus, clearly show that in the region of the PDR (between 5.0 and 8 MeV) most states have the characteristic E1 behavior. A similar analysis was made for the nucleus ^{124}Sn as reported in [71]. Gamma decay of M1 type was not identified with the $(^{17}\mathrm{O}, ^{17}\mathrm{O}'\gamma)$ data and this is consistent with the fact that, at 20 MeV/u, this reaction has a strong isoscalar character and thus it populates primarily natural parity states, namely 1^- and 2^+.

Concerning high-lying 2^+ states, in the case of ^{124}Sn $(^{17}\mathrm{O}, ^{17}\mathrm{O}'\gamma)^{124}\mathrm{Sn}^*$ several states were found in the excitation energy region between 3 to 5 MeV and their analysis is in [94]. Only a few of these states were identified in (γ, γ').

5.2 Isospin mixing

When an isoscalar 1^- state is excited by the isoscalar field of a probe with dominant isoscalar character, the E1

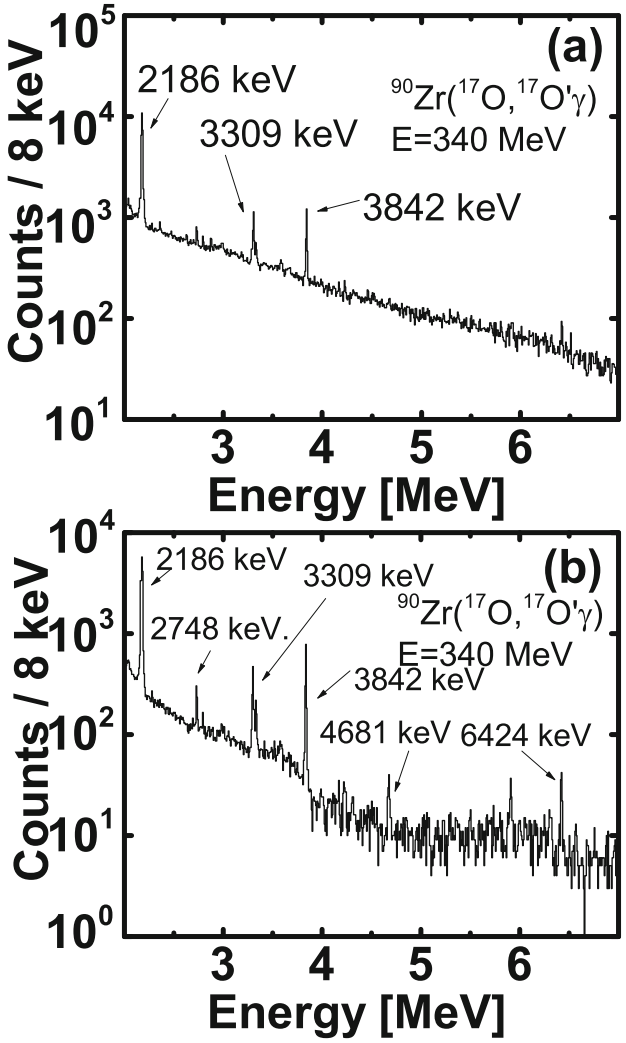

Fig. 12. Panel (a): γ-ray energy spectrum in the 2–7 MeV interval, measured with the AGATA array and corresponding to the ^{17}O scattering channel for ^{90}Zr. Panel (b): γ-ray energy spectrum in the same interval, corresponding to the ^{17}O scattering channel for ^{90}Zr with the additional condition of selecting the deexciting transitions to the ground state. Adapted from [73].

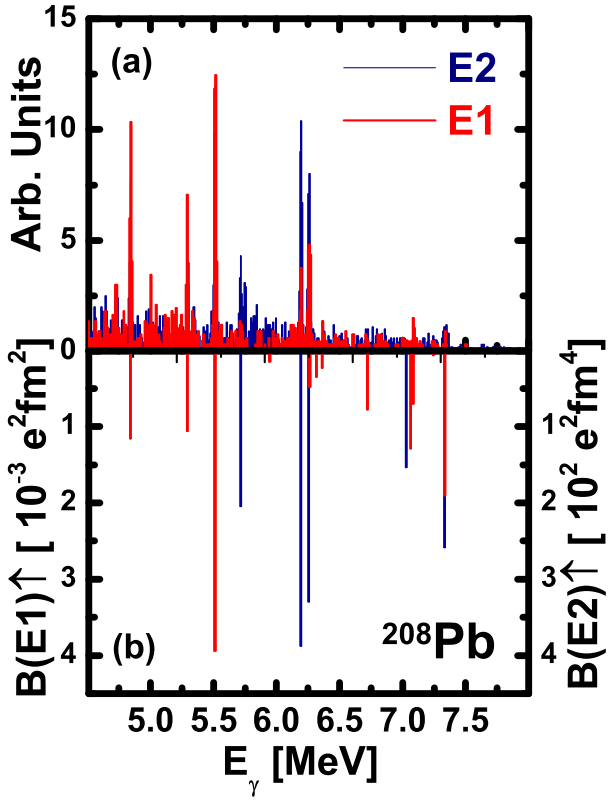

Fig. 13. (Color online) Panel (a): Gamma-ray spectra for ^{208}Pb displayed in the 4.5–8 MeV region, with a condition on the angle between the emitted γ-ray and the recoil direction which enhances the E1 decays (red line) and E2 decays (blue line). Panel (b): The B(E1)↑ (red bars) and B(E2)↑ (blue bars) strength distributions, obtained in (γ,γ') experiments [92,93].

gamma decay, which must proceed through the isovector part of the E1 transition operator, is possible because of the presence of isospin impurities in the state. It is found that the isospin admixtures become more important with increasing excitation energy. This possibly indicates that an important role is played by the IVGDR in introducing isospin admixtures into the isoscalar dipole states. Since isospin mixing is expected to impact the dipole response it is worthwhile to investigate it more in detail. For this purpose one should examine the cross section population for 1^- states closely lying in energy which are almost pure in isospin character. In this case a determination of the isospin-mixing interaction becomes possible. If one assumes a two-state isospin mixing with initially unperturbed pure isovector IV and isoscalar IS states, a square mixing amplitude denoted with $\beta_{\rm mix}$ can be obtained from the B(E1)↑ of these states. Indeed, by using the two state mixing approach induced by an interaction denoted by V one of the two mixing amplitudes $\beta_{\rm mix}$ is obtained from the ratio

$$\beta^2_{\rm mix} = \frac{\mathrm{B(E1)}\uparrow_{\rm II}}{\mathrm{B(E1)}\uparrow_{\rm I} + \mathrm{B(E1)}\uparrow_{\rm II}}\,, \tag{6}$$

where I/II denotes the perturbed almost pure IV/IS state, whose energy difference is given by ΔE_p. The latter is deduced from the experimental data as $\Delta E_p = E_{\rm I} - E_{\rm II}$. The quantity $\beta_{\rm mix}$ can be deduced also from (γ,γ') experiments. The other mixing amplitude $\alpha_{\rm mix}$ is obtained from the normalization condition

$$\alpha^2_{\rm mix} + \beta^2_{\rm mix} = 1. \tag{7}$$

Denoting with $\Psi_{\rm I,II}$ the wave function of the perturbed state and with $\Phi_{1,2}$ that of the unperturbed pure IV/IS state, one gets their relation in terms of the mixing amplitudes $\alpha_{\rm mix}$ and $\beta_{\rm mix}$:

$$\Psi_{\rm I} = \alpha_{\rm mix}\Phi_1 + \beta_{\rm mix}\Phi_2 \tag{8}$$

$$\Psi_{\rm II} = -\beta_{\rm mix}\Phi_1 + \alpha_{\rm mix}\Phi_2. \tag{9}$$

The energies of the states associated to the unperturbed wave function are denoted with E_1 and E_2 and their difference is $\Delta E_u = E_1 - E_2$. Consequently the difference

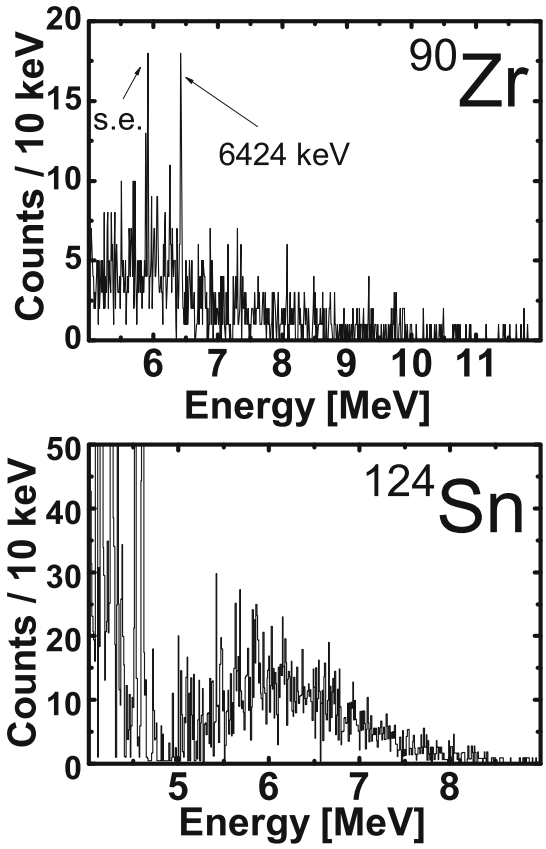

Fig. 14. Top panel: ^{90}Zr γ-ray energy spectrum in the 5–12 MeV interval corresponding to the ^{17}O scattering channel, selecting the de-exciting transitions to the ground state and with the additional condition on the angle between the emitted γ-ray and the recoil direction, which enhances the E1 component. The peak corresponding to the single escape (s.e.) from pair production for the 6424 keV transition is indicated with an arrow. Lower panel: γ-ray energy spectrum of ^{124}Sn in the PDR region obtained with the gating conditions selecting the transitions to the ground state. Adapted from [73] and [71].

between the perturbed (measured value) and the unperturbed energy is given by $|\Delta E_s| = |E_{\rm II} - E_2| = |E_{\rm I} - E_1|$. To extract the numerical value of the mixing interaction V and of the difference between the perturbed and unperturbed energy ΔE_s one can use the following equations [95]. Defining R as

$$R = \frac{\Delta E_u}{V}\,, \tag{10}$$

one can express $\beta_{\rm mix}$ in terms of R and the corresponding dependence is

$$\beta_{\rm mix} = \frac{1}{1 + \quad R/2 + \quad \sqrt{1 + \frac{R^2}{4}}\Big]^{2}}^{\frac{1}{2}}. \tag{11}$$

This equation was used to obtain the values reported in table 4. The relationship between the unperturbed and perturbed energy differences among the two states can

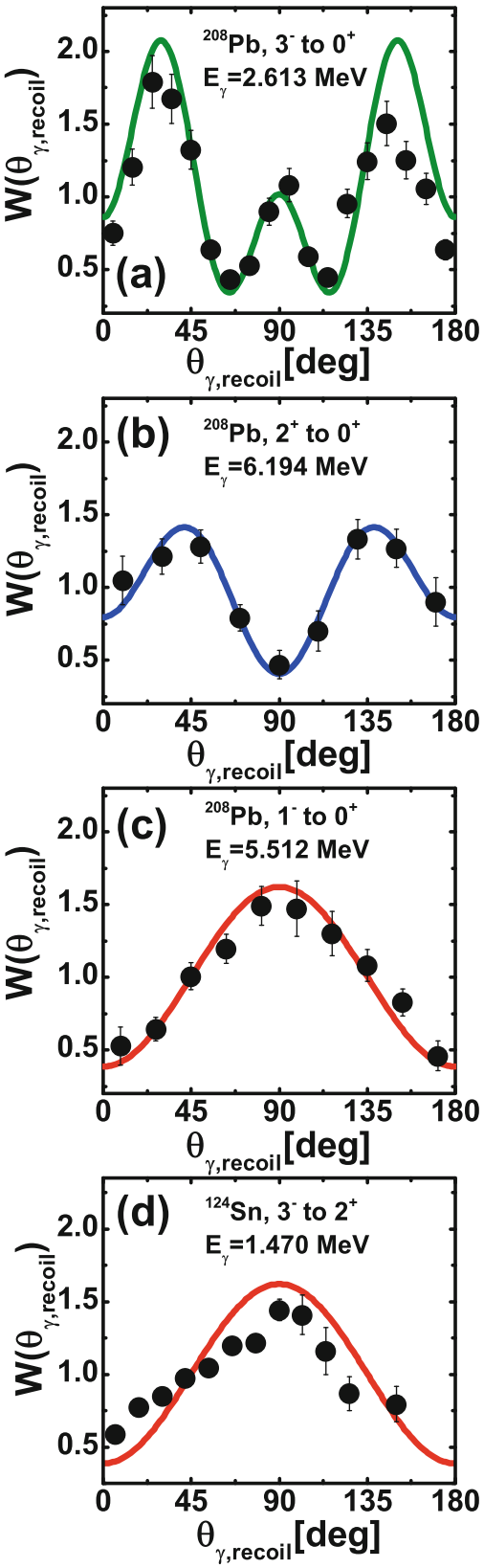

Fig. 15. (Color online) Panels (a)–(c): The angular distributions of γ-ray transitions of ^{208}Pb with different multipolarities. Panel (d): The angular distribution of the E1 γ-ray transition from the 3^- state at 2.602 MeV to the 2^+ state at 1.132 MeV of ^{124}Sn.

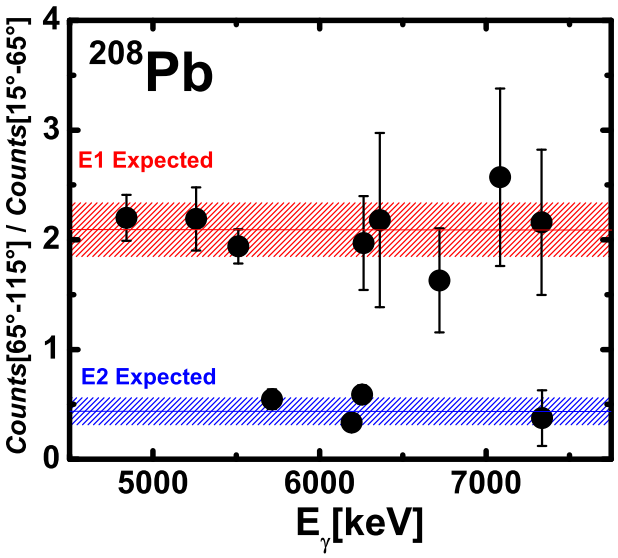

Fig. 16. (Color online) Ratio between the number of counts in the 65°–115° angular interval over the number of counts in the 15°–65° angular interval measured for different transitions of ^{208}Pb. The horizontal red and blue bands correspond to the expected ratio for E1 and E2 transitions, respectively.

Table 4. This table gives the isospin-mixing interaction V, the quantity R defined in the text depending on $\beta_{\rm mix}$ and the energy of the states measured in the experiment (and thus the perturbed energy).

Isotope	V (keV)	R	Reaction	Energy (MeV)	Ref.
^{48}Ca	85(3)	3.67	$(\alpha,\alpha'\gamma)$	7.3,7.6	[62]
^{90}Zr	41.2	0.46	$(^{17}\mathrm{O},{}^{17}\mathrm{O}'\gamma)$	6.30,6.42	[73]
^{90}Zr	73.0	2.76	$(^{17}\mathrm{O},{}^{17}\mathrm{O}'\gamma)$	6.57,6.76	[73]
^{208}Pb	11.6	0.62	$(^{17}\mathrm{O},{}^{17}\mathrm{O}'\gamma)$	7.06,7.08	[70]

also be expressed in terms of R,

$$\Delta E_p = E_{\rm II} - E_{\rm I} = \Delta E_u \quad \sqrt{1+\frac{4}{R^2}}. \qquad (12)$$

Using the experimental values of ΔE_p and $\beta_{\rm mix}$ the value of the interaction V and ΔE_s were extracted for few 1^- states in the region of the pygmy dipole resonance. They are reported in table 4. These values are obtained for two pairs of transitions in ^{90}Zr and one pair of transitions in ^{208}Pb which are shown in fig. 17. In addition, the data for ^{48}Ca from [62] are given in the same table.

This analysis provides useful indication for the isospin mixing between 1^- states very far off yrast and in the energy region of the pygmy dipole resonance which are particularly relevant for the understanding in what way isospin is broken for the eventual formation of neutron skin oscillations about an isospin symmetric core. It is interesting to note that in the case of ^{48}Ca this isospin-mixing matrix element between far off yrast states is already one order of magnitude larger than the one found at yrast in

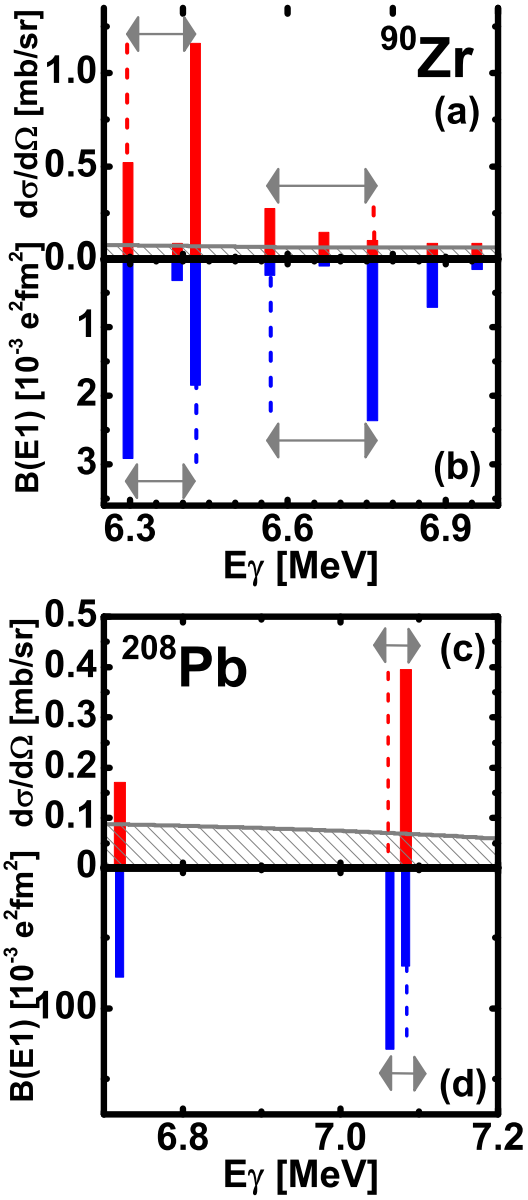

Fig. 17. Top panel: Cross section for the excitation of 1^- states in ^{90}Zr deduced from the $(^{17}\mathrm{O},{}^{17}\mathrm{O}'\gamma)$ experiment (red bars (a)), in comparison with the B(E1) strength distribution (blue bars (b)). The grey solid line represents the sensitivity limit. Pairs of close-lying states appearing to be almost pure in isospin character and for which the isospin-mixing matrix element has been deduced (see text) are indicated with the grey arrows. Bottom panel: The same as above for ^{208}Pb.

the odd-odd $N = Z$ nucleus ^{54}Co with about the same mass but even larger proton number.

5.3 DWBA analysis of the excitation cross section

The measured cross sections for elastic scattering (^{17}O, ^{17}O) and for states identified with the $(^{17}\mathrm{O},{}^{17}\mathrm{O}'\gamma)$ reaction were analyzed using the Distorted Wave Born Approximation approach (DWBA). This approach assumes

Table 5. Optical model parameters. V and W are the strengths of the real and imaginary potentials (in MeV); $r_0 = r_V = r_W$ (in fm) is the radius parameter; $a = a_V = a_W$ (in fm) is the diffusness parameter; r_C is the Coulomb radius.

Reaction	V (MeV)	W (MeV)	r_0 (fm)	a (fm)	r_C (fm)	Ref.
^{17}O + ^{90}Zr at 20 MeV/u	40	26	1.15	0.671	1.20	[73]
^{16}O + ^{90}Zr at 25 MeV/u	40	26	1.15	0.671	1.20	[98]
^{17}O + ^{124}Sn at 20 MeV/u	50	32	1.16	0.670	1.20	[71]
^{17}O + ^{208}Pb at 20 MeV/u	40	42.5	1.15	0.767	1.20	[70]
^{17}O + ^{208}Pb at 22 MeV/u	40	42.5	1.15	0.767	1.20	[78]

a direct reaction process and requires as main ingredients an optical model to describe the incoming and outgoing waves and a form factor containing the nuclear structure aspects of the reaction. The very widely used code FRESCO [96, 97] was used to perform this type of calculations. For the elastic scattering differential cross section (^{17}O, ^{17}O) the optical-model potential was assumed to be of Woods-Saxon form

$$U(r) = -Vf(x_\nu) - iWf(x_W), \tag{13}$$

with

$$f(x_i) = (1 + e^{x_i})^{-1}, x_i = (r - R_i)/a_i \tag{14}$$

$$R_i = r_i(A_p^{1/3} + A_t^{1/3}), \tag{15}$$

with $i = V, W$. The Coulomb potential was taken to be that of a point charge interacting with a uniform charge distribution with radius $R_C = r_C(A_p^{1/3} + A_t^{1/3})$ fm. In the calculations made for elastic cross section the values of the optical potential parameters, for the real and imaginary terms, were deduced from the best fit to the experimental data. In table 5 the optical model parameters deduced from the experimental cross sections of the elastic scattering process are given. The values are in agreement with the ones reported in [74, 78, 98] and references therein. They are also given in table 5 for ^{90}Zr, ^{208}Pb. The values of the Coulomb radius parameter R_C are also reported in the table. For each measured nucleus an overall experimental normalization was obtained by imposing the measured elastic scattering yield at small angles to be equal to the calculated cross sections (for example, in the case of ^{90}Zr the normalization was at $\theta = 9.4°$ in the centre-of-mass frame). The normalization value was deduced for each target using the elastic scattering data and accounts for the combined effect of the integrated current (for which we did not have a precise measurement), target thickness and dead time. To be noted that the error for each experimental point was determined by combining the statistical error with the uncertainty in the solid angle related to each pixel. The latter is an important contribution at the most forward angles where the statistics is high. The value of the total uncertainty varies between 10% and 17%. The average deviation from the data to the calculations when normalized at the most forward angle is smaller than the total uncertainty in the data, namely is between 9% to 13% depending on the target nucleus. To gain confidence on this normalization, calculations were made with the FRESCO code for the elastic scattering data in literature on ^{90}Zr, ^{208}Pb at slightly higher energy. These calculations reproduced the old data with the same optical model parameters reported in literature [74,78,98]. In fig. 18 the data and optical model calculations for the (^{17}O, ^{17}O) elastic scattering cross section for ^{90}Zr, ^{208}Pb, and ^{124}Sn are shown. One can see that in all cases the experimental points are well reproduced by calculations over the entire measured angular interval. In the bottom part of fig. 18 elastic scattering data at $\theta = 14.0°$ for the three targets are shown displaying a rapid variation of the nuclear cross section.

For each nucleus the analysis of cross sections for excited states used the associated optical model parameters and the normalization deduced from elastic scattering multiplied by the γ-ray detection efficiency (varying for the different experiments and, *e.g.*, being 2.9% at 2.186 MeV for the ^{90}Zr case). To be noted that for each nucleus no further normalization was applied when comparing data associated to excitation of different states with predictions.

The differential cross sections as a function of angle for exciting the collective states of different multipolarities were also calculated using the distorted wave approximation approach. In addition some calculations were made using the exact coupled-channel method. No substantial difference was found when comparing the two types of calculations and this indicated that the effects of coupling to the elastic channel are unimportant. Nuclear transition potentials for angular momentum transfer L to the nucleus are assumed to have the form

$$H_L^N(r) = -\delta_V(L)\frac{\mathrm{d}V(r)}{\mathrm{d}r} - i\delta_W(L)\frac{\mathrm{d}W(r)}{\mathrm{d}r}\,, \tag{16}$$

where $V(r)$ and $W(r)$ are the real and imaginary parts of the optical potential used for the fits to the elastic data. In the analysis the real and imaginary deformation lengths are assumed to be equal, $\delta_V(L) = \delta_W(L) = \delta_L$.

The Coulomb interaction is represented in the form of a multipole expansion between a point charge and a uniformly charged sphere with radius R_C, *i.e.*,

$$H_L^C(r) = \frac{4\pi Z_p e}{2L+1}[B(EL)]\uparrow^{1/2} F, \tag{17}$$

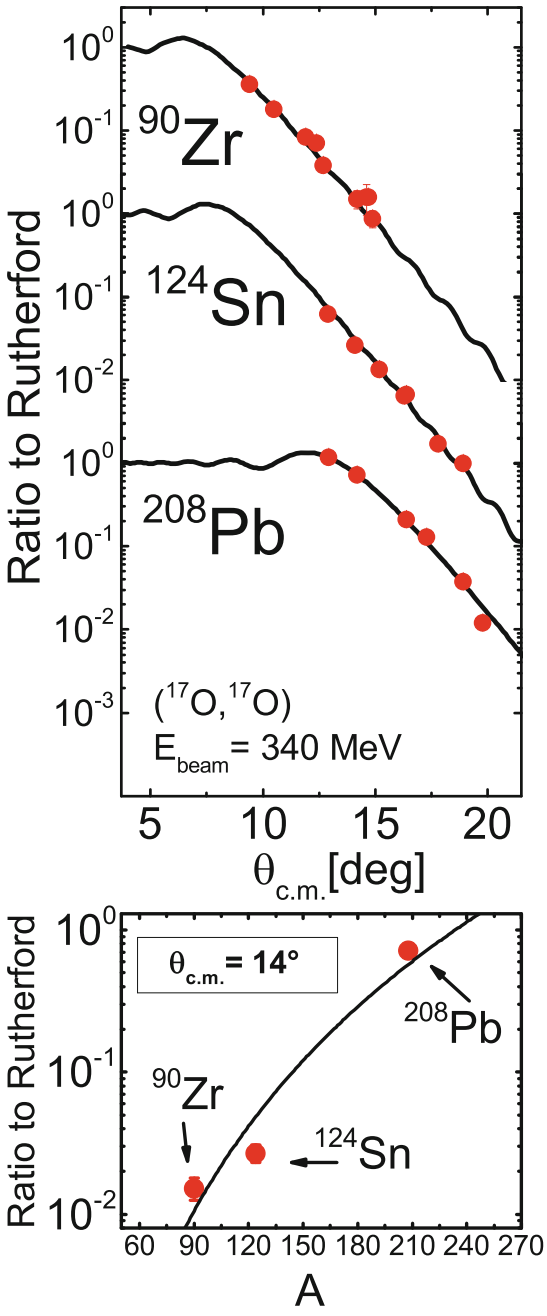

Fig. 18. (Color online) Top panel: The $(^{17}O, ^{17}O)$ elastic-scattering differential cross section measured in the center-of-mass frame and divided by the Rutherford cross section is shown for ^{90}Zr, ^{124}Sn and ^{208}Pb (red dots). Optical model calculations are displayed with black solid curves. Adapted from [71, 73, 94] Bottom panel: Cross section data at $\theta = 14°$ for the three nuclei measured at the same bombarding energy. The black solid line represents an interpolation (power type).

with

$$F = \frac{r^L}{R_C^{2L+1}}; r < R_C \tag{18}$$

and

$$F = 1/r^{L+1}; r \geq R_C. \tag{19}$$

In the expression above Z_p is the atomic number of the projectile and $B(EL)\uparrow$ is the charge multipole moment. The used deformed potential model assumes that the deformaton length of the transition potential is equal to that of the nuclear density distribution. The mass multiple moment can then be expressed as

$$B(L)\uparrow = \delta_L^2 \left[\frac{3A}{4\pi} R^{L-1}\right]^2, \tag{20}$$

if a uniform distribution with radius R is assumed. One can also write the mass multiple moment in terms of the r^L radial moments of the neutron and proton transition densities, *i.e.*,

$$B(L)\uparrow = |M_n + M_p|^2. \tag{21}$$

Since $B(EL)\uparrow = |M_p|^2$, one finds

$$\left|\frac{M_n}{M_p}\right| = \left[\frac{B(L)\uparrow}{B(EL)\uparrow}\right]^{1/2} - 1, \tag{22}$$

which is an indication of the isospin character for the excitation. For multipoles with $L \geq 2$, the deformation length δ_L corresponding to 100% of the isoscalar energy-weighted sum rule (EWSR) is given by the relation

$$\delta_L^2 = 2\pi\hbar^2 \frac{L(2L+1)}{3mAE_x}, \tag{23}$$

where m is the nucleon mass, A the mass number, and all the strength is assumed to be localized at an excitation energy E_x.

The magnitude and shape of the differential cross section are dependent upon the magnitude of the nuclear and Coulomb amplitudes as well as their relative phase. In principle, one can determine two quantities by comparing the calculations with the data, *e.g.*, δ_L (or M_n/M_p) and $B(EL)\uparrow$. In the analysis of the data presented here the values $B(EL)\uparrow$ were taken from other works, mainly from (γ, γ') data.

5.4 Results for 2^+ and 3^- states

In order to obtain a consistent overall picture from the adopted analysis procedure it is important, before concentrating on the 1^- states, which are the main focus of this paper, to discuss some results for 2^+ and 3^- states. In figs. 19–23 data for ^{90}Zr, ^{124}Sn and ^{208}Pb are shown. In the case of high-lying 2^+ states in ^{208}Pb, shown in fig. 23, the measured cross sections are presented in the top panel in comparison with the B(E2)$\uparrow$ values shown in the bottom panel. The corresponding DWBA calculations are also shown in figs. 19 and 20. For these DWBA calculations the values of the reduced transition probability B(E3)$\uparrow$ and B(E2)$\uparrow$ are known from either (γ, γ') and/or lifetime measurements. The calculations assume $M_n/M_p = N/Z$ as for pure isoscalar states. The calculations reproduce quite well the measured cross sections and

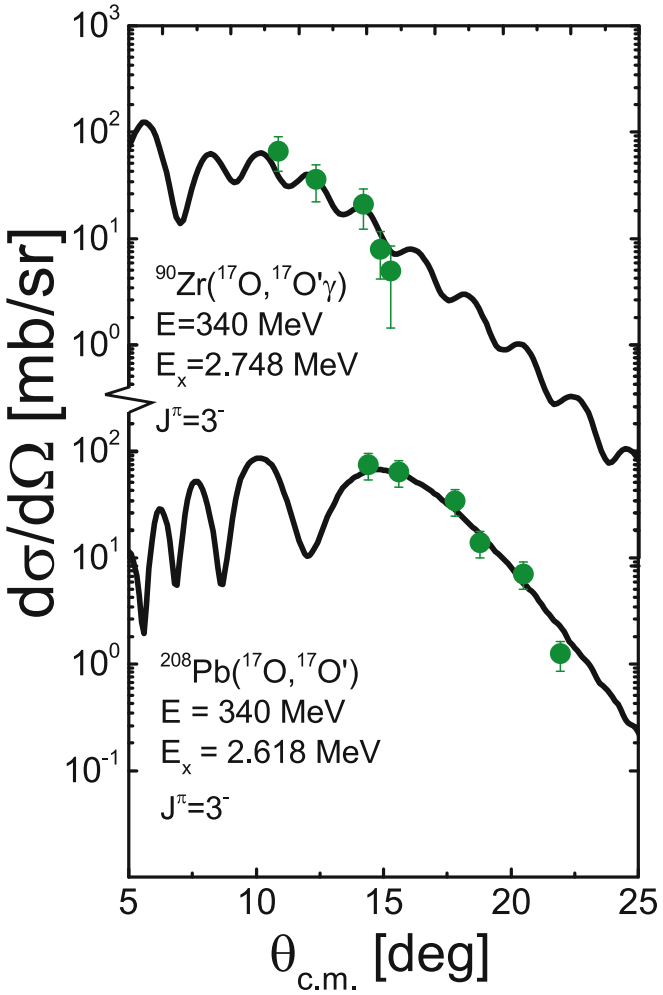

Fig. 19. (Color online) Measured differential cross section $(^{17}\mathrm{O}, ^{17}\mathrm{O}'\gamma)$ at $E_{\mathrm{Beam}} = 340\,\mathrm{MeV}$ for the 3^- states at 2.748 MeV and at 2.618 MeV in ^{90}Zr and ^{208}Pb, respectively. The error bars shown with the data points represent the statistical error. The solid line curves are the predictions obtained with the DWBA approach. Adapted from [71, 73].

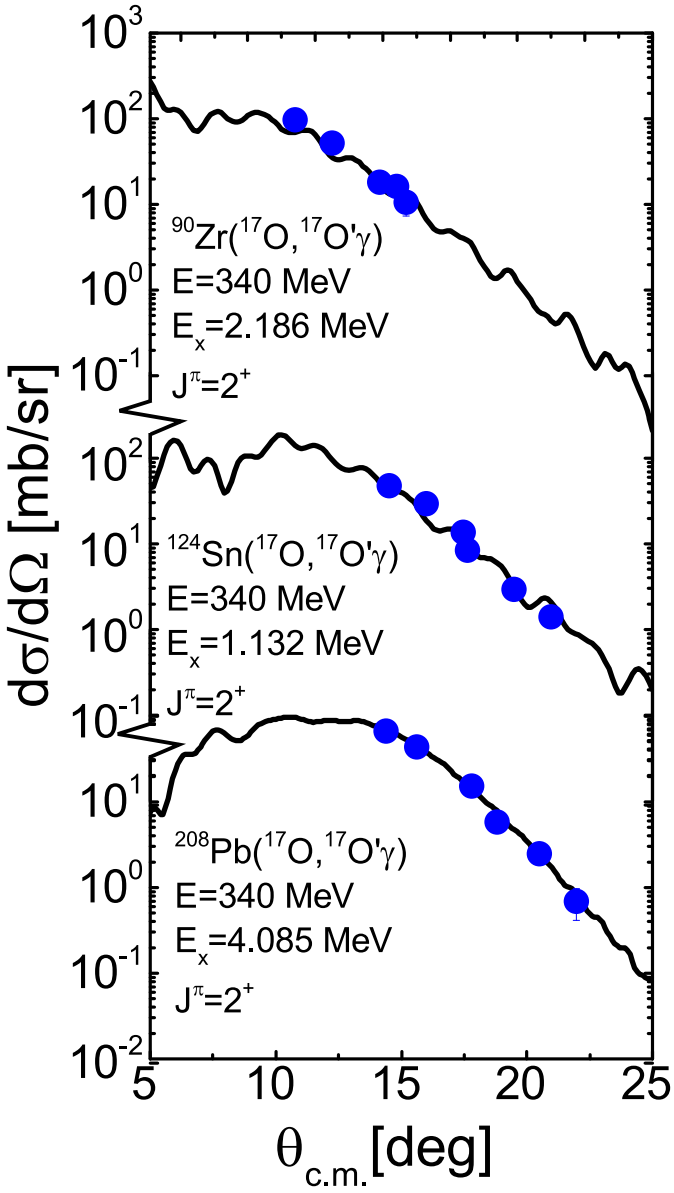

Fig. 20. (Color online) Measured differential cross section $(^{17}\mathrm{O}, ^{17}\mathrm{O}'\gamma)$ at $E_{\mathrm{Beam}} = 340\,\mathrm{MeV}$ for the 2^+ states at 2.186 MeV, 1.132 MeV and 4.085 MeV of ^{90}Zr, ^{124}Sn and ^{208}Pb, respectively. The error bars shown with the data points represent the statistical error. The solid line curves are the predictions obtained with the DWBA approach. Adapted from [70, 71, 73].

this is an indication of the validity of the deformed potential model approach. Only in the case of the 3.842 MeV state in ^{90}Zr it is not possible to reproduce the data by using the standard deformed potential model approach (in fig. 21 calculations for different form factors and different values of M_n/M_p are given as described in the corresponding figure caption). The unusual and not realistic value $M_n/M_p = 0.1 * N/Z$ has been chosen to have a hint on the importance of the nuclear interaction in this excitation process. The reason is related to the complex structure of this state having a strong four-quasi-particle component [99] and therefore it cannot be populated by a one step process as that assumed within the DWBA approach. Indeed a calculation considering only Coulomb excitation (using the measured B(E2)) reproduces the data since it ensures the correct direct excitation via the Coulomb potential while the nuclear potential does not play a significant role in the direct excitation process of such a complex excitation mode. More details are in [73].

For the nucleus ^{208}Pb it is important to point out that the state at 6.194 MeV (shown in fig. 22), seen in the past with electromagnetic probes, was identified for the first time with a hadron probe with the $(^{17}\mathrm{O}, ^{17}\mathrm{O}'\gamma)$ scattering [73]. Presently there is interest in studying also states of different multipolarity in the energy region of the PDR. Indeed an obvious question, arising immediately in this context, is to what extent the presence of a neutron or proton skin will affect excitations of other multipolarities and vice versa. Promising candidates are low-energy 2+ states.

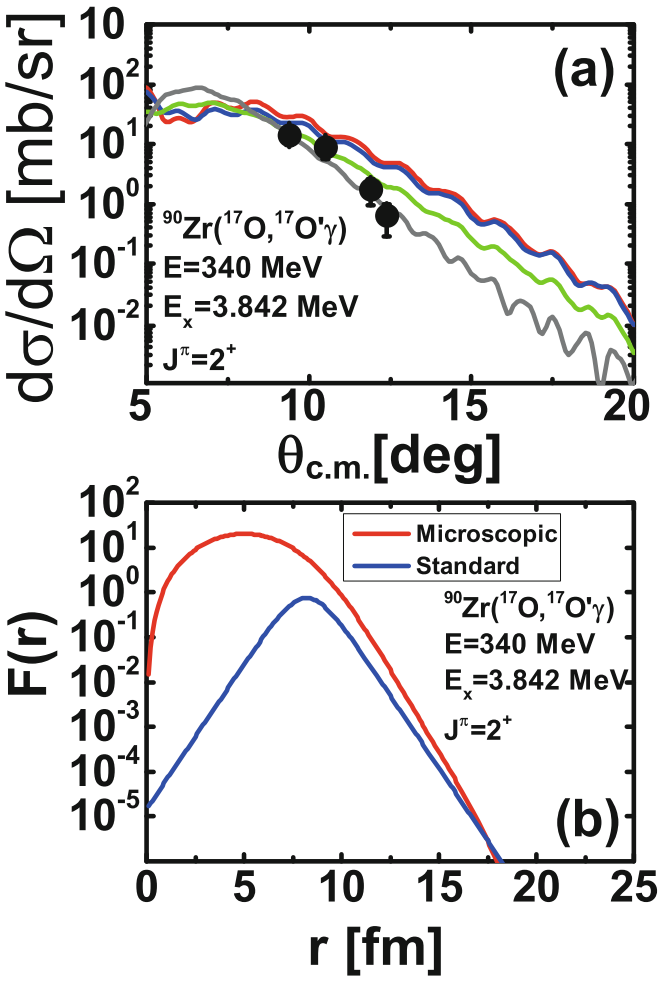

Fig. 21. (Color online) Inelastic scattering cross section ^{90}Zr $(^{17}\mathrm{O}, ^{17}\mathrm{O}'\gamma)^{90}\mathrm{Zr}^*$ at 340 MeV for the 2^+ state at 3.842 MeV (black solid circles). The error bars are the statistical errors. The lines show DWBA calculations. The blue solid curve is the calculation with the standard phenomenological form factor (displayed in panel (b), blue line). The red solid line include the nuclear contribution calculated with the microscopic form factor shown in panel (b) (red line). The DWBA calculations performed with the standard phenomenological form factor but considering $M_n/M_p = 0.1{*}N/Z$ (green line) are displayed. The gray curve represents the calculation performed considering only the Coulomb excitation. Adapted from [73].

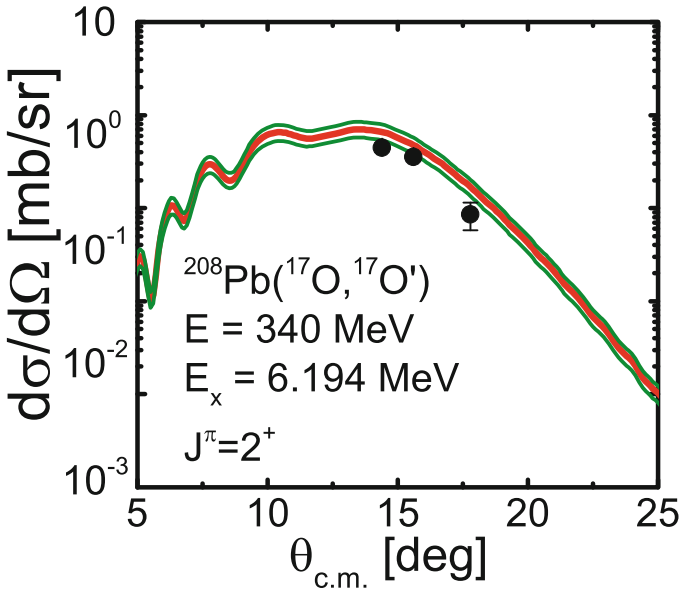

Fig. 22. (Color online) Inelastic scattering cross section ^{208}Pb $(^{17}\mathrm{O}, ^{17}\mathrm{O}'\gamma)^{208}\mathrm{Pb}^*$ at 340 MeV for the 2^+ state at 6.194 MeV (black solid circles) and DWBA prediction (red solid curve). The error bars represent the statistical error. The green solid curves take into account the experimental error in the B(E2)↑ value known from (γ, γ') [92, 93]. Adapted from [70].

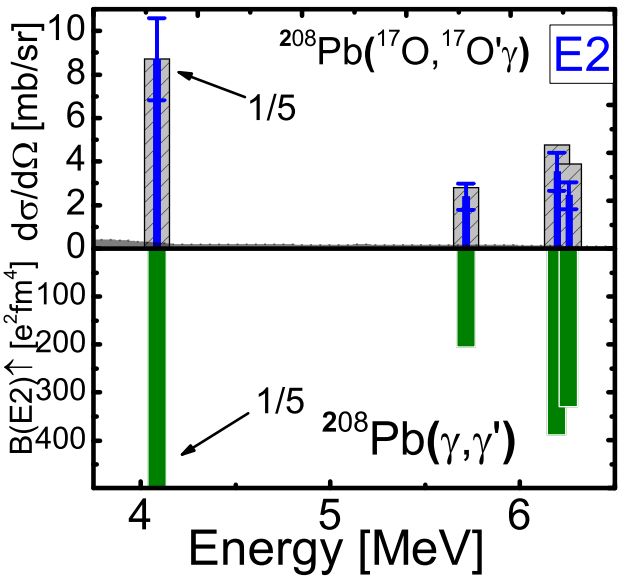

Fig. 23. (Color online) Top panel: The measured differential cross section at the average angle of 15.6° for E2 transitions (blue bars). The dashed gray bars give calculated DWBA excitation cross sections using the B(E2)↑ values known from (γ, γ') and standard form factors (see text). The shaded areas show the sensitivity limit of the experiment. The statistical error of the experiment implies lower and upper values indicated with the short horizontal bars. Bottom panels: electromagnetic reduced transition strength measured with (γ, γ') experiments [93]. Adapted from [70].

The present results suggest a strong isoscalar character for the 2^+ in ^{208}Pb. The finding $M_n/M_p = N/Z$ for these 2^+ states gives constraints to theories predicting in detail the various excitation modes of the nuclear skin. The analysis of the more numerous 2^+ states in ^{124}Sn is in [94]. For neutron-rich Sn isotopes calculations reported in [100] for 2^+ states predict that the spectral distributions, electric quadrupole response functions and transition densities of low-energy quadrupole states show special features generated by the motion of neutron or proton skins.

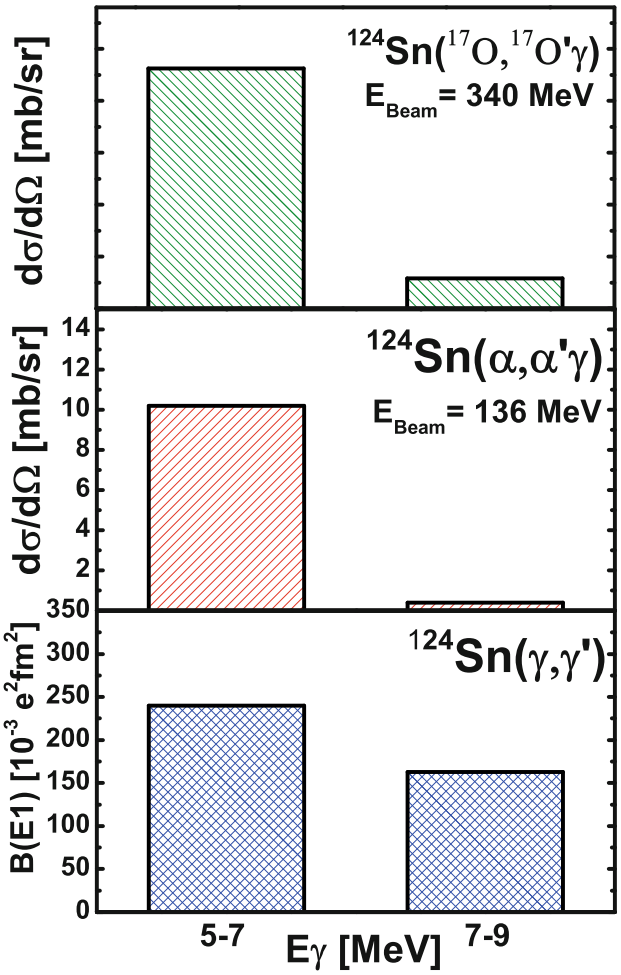

Fig. 24. (Color online) Differential cross sections measured in the ^{124}Sn(^{17}O, ^{17}O$'\gamma$) experiment, corresponding to the discrete lines integrated in two regions 5–7 and 7–9 MeV (top panel). For comparison, the corresponding strengths measured in α-scattering (middle panel) [61] and photon-scattering (bottom panel) [60] are reported. Adapted from [71].

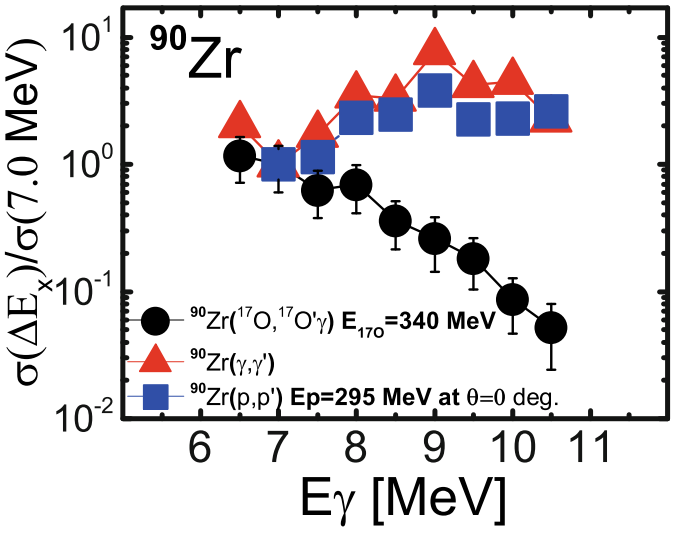

Fig. 25. (Color online) The quantity $\sigma_R = \sigma(E_X)/\sigma(7.0\,\mathrm{MeV})$ in 0.5 MeV bins as a function of excitation energy, for the reactions (^{17}O, ^{17}O$'\gamma$) (black solid circles), and deduced from (γ,γ') data (red triangles) [101] and from (p, p$'$) E1 data (blue solid squares) from ref. [102]. The lines are to guide the eyes and the error bars the statistical uncertainties. Adapted from [73].

5.5 The isoscalar strength in the pygmy region

As in the case of the $(\alpha,\alpha'\gamma)$ data the (^{17}O, ^{17}O$'\gamma$) data show that the population cross section of the high-energy part of the pygmy state distribution is much quenched as compared with the data obtained with the (γ,γ') reaction or with the excitation of virtual photons. This quenching is shown in figs. 24 and 25. Figure 24 gives the comparison for the ^{124}Sn nucleus of the cross section data for the $(\alpha,\alpha'\gamma)$, the (^{17}O, ^{17}O$'\gamma$) and the (γ,γ') reactions. Both the hadron probes excite strongly only the low-energy region of the pygmy states, in contrast with the electromagnetic probes. Figure 25 shows for the ^{90}Zr nucleus the comparison of the cross sections measured at $E_x > 6.5$ MeV with the (^{17}O, ^{17}O$'\gamma$), the (γ,γ') and (p, p$'$) reactions. For this purpose the quantity $\sigma_R = \sigma(E_x)/\sigma(7\,\mathrm{MeV})$, where $\sigma(E_x)$ is the cross section at excitation energy E_x, has been evaluated for these three reactions. This quantity (equal to 1 at 7 MeV) is given in bins 0.5 MeV wide and the error bars in the cases of the (γ,γ') and (p, p$'$) data are smaller than the symbols and for the (^{17}O, ^{17}O$'\gamma$) data reflect the statistical uncertainties. A strong increase of these relative cross sections in the excitation energy interval 6.5 to 11 MeV is observed in the case of the (γ,γ') and (p, p$'$) data, the latter obtained at 295 MeV at zero degree where the Coulomb field is dominant and thus related to virtual photon excitation. In contrast, a strong decrease is evident in the (^{17}O, ^{17}O$'\gamma$) data. This is a further indication of the separation in two distinct parts of the low-lying dipole region: one which is populated by both isoscalar and isovector probes and the other one, at higher energy, where only the electromagnetic interaction excites these states. More data, also obtained using other types of reactions, with higher statistics and small energy bins are needed to get a better insight into the nature of 1^- states particularly in the energy region where a transition between pygmy states and GDR-type states occurs, namely at around 10 MeV.

One relevant and general finding from analyses for the excitation of 1^- states obtained with the (^{17}O, ^{17}O$'\gamma$) reaction is the impossibility to reproduce most of the data with DWBA calculations that treat these states as of GDR type. For the measured 1^- states the values of B(E1)↑ from (γ,γ') data were used. In the case of the ^{17}O probe at the bombarding energy of 20 MeV/u the computed Coulomb contribution to the cross section was found to be in average of the order of 10%. In addition, the isovector part of the nuclear interaction is much smaller than the isoscalar part.

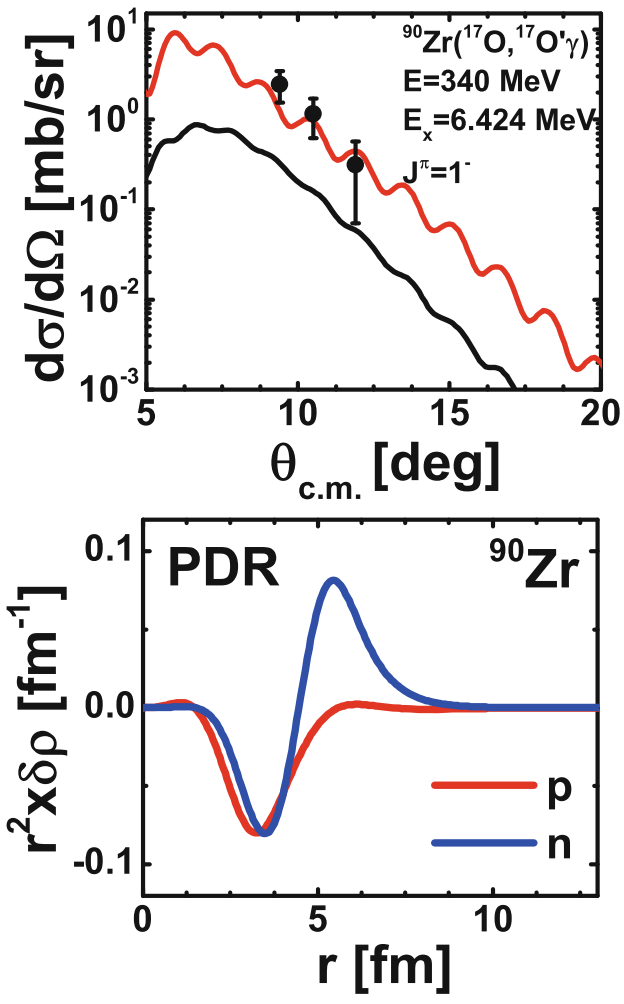

Fig. 26. (Color online) (Top) Inelastic scattering cross section ^{90}Zr(^{17}O, ^{17}O′γ)^{90}Zr* at 340 MeV for the 1$^-$ state 6.424 MeV. The error bars are the statistical errors. The lines show DWBA calculations. The black solid curve represents the calculations with the standard phenomenological form factor. The red solid line includes the nuclear contribution calculated with the microscopic form factor (see text) derived with the transition density shown in the bottom panel. Adapted from [73].

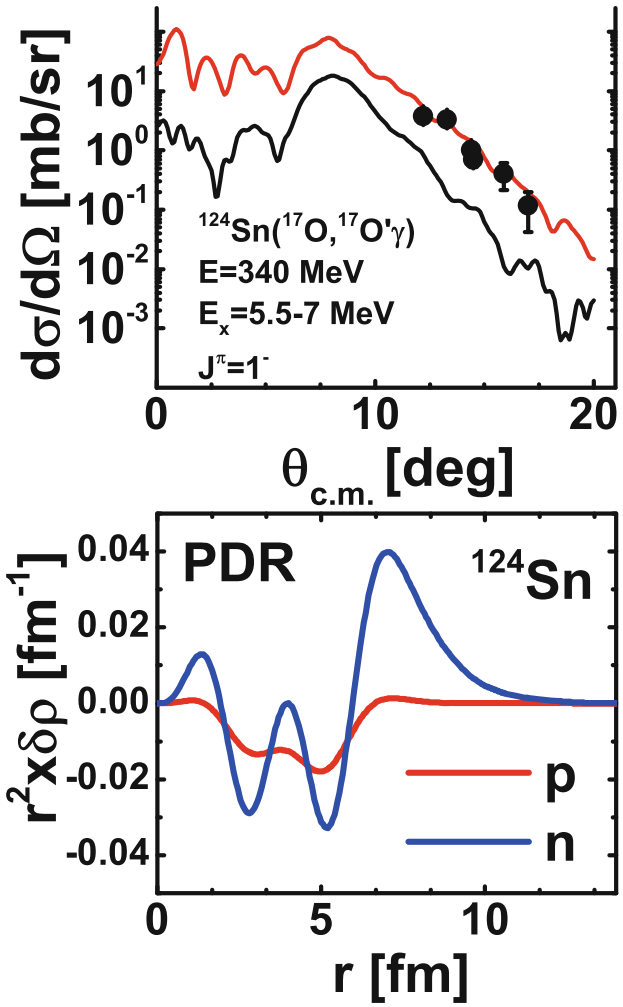

Fig. 27. (Color online) (Top) Inelastic scattering cross section ^{124}Sn(^{17}O, ^{17}O′γ)^{124}Sn* at 340 MeV for the 1$^-$ states between 5.5–7 MeV. The error bars are the statistical errors. The lines show DWBA calculations. The black solid curve represents the calculations with the standard phenomenological form factor. The red solid line includes the nuclear contribution calculated with the microscopic form factor (see text) derived with the transition density shown in the bottom panel. Adapted from [71].

In the following we denote as "DWBA-standard" the calculations that treat 1$^-$ states as pure-isovector states and use for the nuclear part (whose calculated cross section is however very small) a rather crude approach, namely deformed potentials of the same type used for states with higher multipolarities. In figs. 26, 27 and 28 some selected data for 1$^-$ states for ^{90}Zr, ^{124}Sn and ^{208}Pb are shown together with predictions of "DWBA-standard" type (black solid lines). The comparison of the data with calculations, obtained assuming the 1$^-$ states to have a dominating isovector character, suggests that the part of the cross section due to the nuclear interaction is not treated properly in those calculations. In the case of ^{90}Zr, which has a rather high value of the neutron binding energy, one has learned from [73] that a very poor description of the nuclear part of the cross section concerns all 1$^-$ states up to approximately 10 MeV.

In general it has been found that the "DWBA-standard" calculations are, on the one hand, always smaller than the measured cross sections and, on the other hand, they are mainly equal to the calculations including the Coulomb excitation only. Then, one deduces that the nuclear contribution to the excitation process is important and it has to be included in the cross section calculations in a proper way. Therefore, in order to reproduce the measured cross sections for 1$^-$ states, other DWBA calculations were made adopting radial form factors of microscopic type. These form factors were built using the double folding procedure by employing microscopic RPA transition densities as described in sect. 3. The comparison of the form factors used for the calculations of "DWBA-standard" type with those employing microscopic calcula-

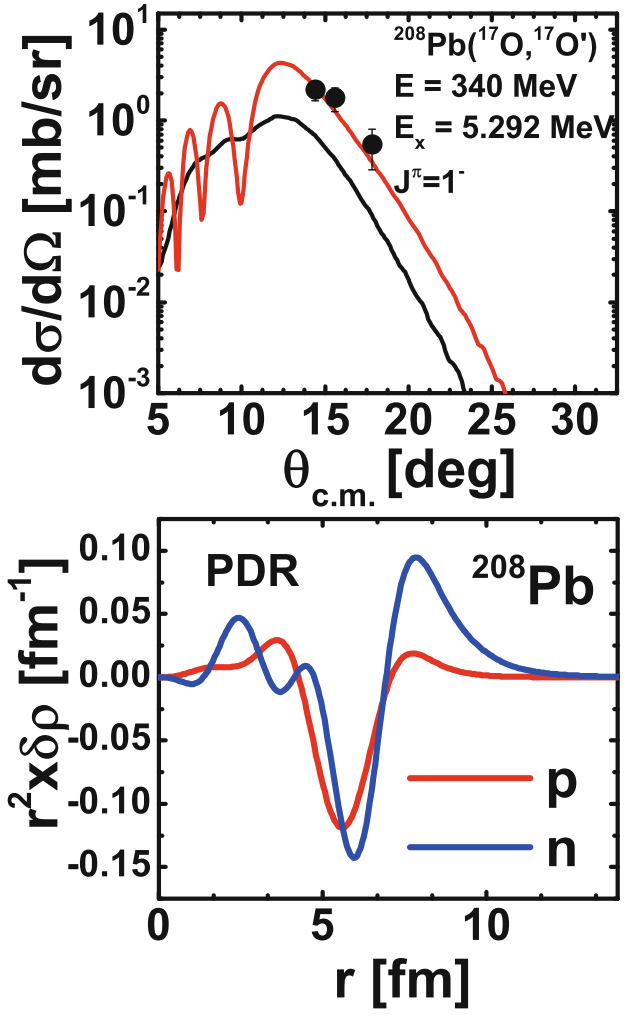

Fig. 28. (Color online) (Top) Inelastic scattering cross section ^{208}Pb(^{17}O, ^{17}O′γ)^{208}Pb* at 340 MeV for the 1^- state 5.292 MeV. The error bars are the statistical errors. The lines show DWBA calculations. The black solid curve represents the calculations with the standard phenomenological form factor. The red solid line includes the nuclear contribution calculated with the microscopic form factor (see text) derived with the transition density shown in the bottom panel.

tions evidences differences both in the nuclear interior and around the nuclear surface. Due to the incident energy employed, the projectile ^{17}O is interacting mainly with the nuclear surface and the DWBA calculations were found to be insensitive to the details of the form factor in the interior of the nucleus. Conversely, the proper description of the form factor around the surface was found to change dramatically the size of the cross section [57].

Predictions obtained using the form factors based on microscopic calculations of the transition densities are shown in comparison with the data in figs. 26, 27 and 28 (red solid lines). As previously discussed it is important to note that in all cases the used transition densities are different for protons and neutrons. They are characterized by an oscillation in phase inside the nucleus and by a concentration of only neutron strength at the surface. Therefore

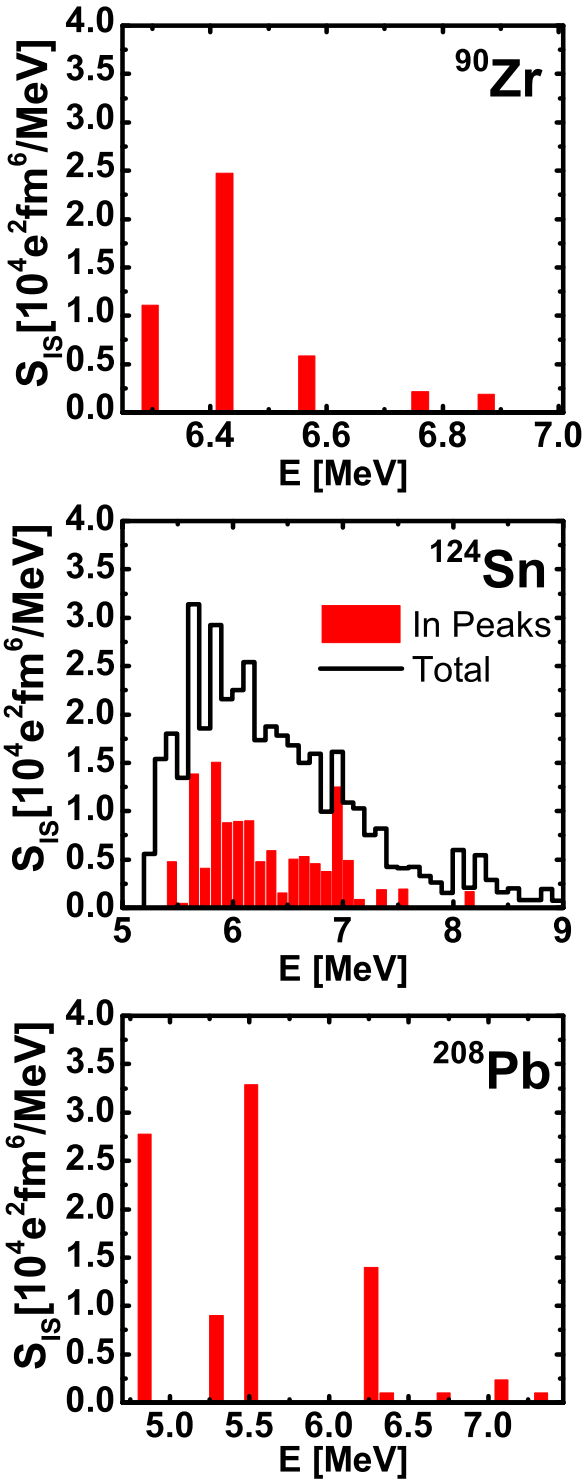

Fig. 29. (Color online) Isoscalar strength distribution measured for the PDR states. The full coloured red bars correspond to the isoscalar strength of the observed known discrete transitions for the case of ^{90}Zr (top) and ^{208}Pb (bottom) and correspond to the sum of known discrete transitions in each energy bin of 100 keV for the case of ^{124}Sn (middle). In the middle panel the black histogram gives the total strength (including the unresolved part) corresponding to the total counts in each energy bin. In all the cases the predicted Coulomb contribution was subtracted.

Table 6. Table of the isoscalar strengths and B(E1)↑.

Isotope	Selection	Energy range [MeV]	Isoscalar strength [10^4 e^2 fm^6/MeV]	Isoscalar EWSR [%]	B(E1)↑ [10^{-3} e^2 fm^2]
^{90}Zr	in peaks	6.3–6.9	4.6(0.7)	4.0(0.6)	87
^{124}Sn	in peaks	5.5–7.0	10.8(1.4)	1.5(0.2)	214
^{124}Sn	in peaks	5.5–9.0	11.9(1.6)	2.2(0.3)	228
^{124}Sn	unresolved	5.5–9.0	41.1(3.7)	7.8(0.7)	228
^{208}Pb	in peaks	4.8–7.3	8.9(1.5)	9.0(1.5)	1084

the good reproduction of the data with these calculations supports the picture that these pygmy states are excitations of the neutron skin. As expected for these states, the dominant contribution to the form factor comes from the isoscalar part of the nucleon-nucleon interaction component. The calculations based on the microscopic form factors were fitted to the data to extract the value of the ISEWSR strength. In particular, it has been assumed that the cross section is a sum of two parts, one being the Coulomb and the other the nuclear (isoscalar) contribution. For the Coulomb contribution we fixed the value corresponding to the known B(E1) measurements. For the nuclear contribution to fit the data, the starting value was that associated to the used microscopic form factor corresponding to a specific fraction of the ISEWSR strength. The extracted values for ^{90}Zr, ^{124}Sn and ^{208}Pb are displayed in fig. 29 and given in table 6 also as a fraction of the ISEWSR E1 strength. In general the deduced values are consistent with the results for the isoscalar giant dipole resonance. In the case of ^{90}Zr new data are needed to extract the strength at energy > 7 MeV characterized by the presence of several weak transitions.

6 Summary

Progress has been made in the detail study of the nature of 1^- states at around the neutron binding energy. This information is attracting interest to test models based on Energy Density Functional used also for astrophysical applications such as those for neutron stars. High-resolution experiments using both hadron and electromagnetic probes are found to be key tools to understand the isospin character of the pygmy states. Isoscalar strengths in general lower than 10% of the corresponding value of the ISGDR at 20–30 MeV were deduced from the analysis of the hadron data with the distorted wave Born approximation approach.

More data are necessary to probe more in detail the shape of the transition density and to deduce the mixing among the isoscalar and isovector components. In particular the study of isoscalar pygmy states in deformed nuclei is very interesting. Like the case for the IVGDR where the oscillation along the two principal axes produces a separation in two peaks of the IVGDR structure, the question is whether also for the low-lying dipole states one can measure such separation. A first attempt in this direction has been performed at RCNP at Osaka where polarized protons at 0° degrees have been used on ^{154}Sm [103]. The overall picture obtained from the available results supports the interpretation of the low-lying pygmy states as due to the excitation of the neutron skin.

In the future, it will be important to address open problems for stable nuclei and to search for 1^- states, with their isoscalar and isovector components, in nuclei far from stability. For stable nuclei the transition between the PDR and GDR regime should be understood (with measurements of gamma decay above particle separation) and information on the nuclear transition density should be obtained in order to provide stringent tests to theory. The gamma decay measurements at energy above particle separation require larger detection efficiency and in the case of the (γ, γ') reaction more intense gamma-ray beams.

For nuclei far from stability measurements using radioactive beams in inverse kinematics should be made. One could consider to use, in addition to liquid H and He targets, also solid targets of ^{13}C for measurements at bombarding energies in the interval 10–20 MeV/u for which the detection of gamma-rays is also made. These bombarding energies will be available at ISOL facilities of new generation such as SPIRAL2 and SPES.

Excitations of the neutron skin with other multipolarities are also expected to exist, particularly of 2^+ type. Up to now weak gamma-ray transitions below 5 MeV from 2^+ states are difficultly identified using the (γ, γ') reaction. This is because of the rather high background characterizing measurements using beams produced with the Bremsstrahlung technique. Conversely, one expects to be able to search for E2 pygmy states by using very intense beams of high quality such as those produced with the inverse Compton technique (*e.g.*, those with very narrow energy band widths that will be available in the future facility ELI_NP).

The authors are grateful to the AGATA Collaboration, the LNL laboratory, and accelerator group at LNL who made the experiments with ^{17}O beams here discussed possible. This work was also supported by "Programma di Ricerca Scientifica di Rilevante Interesse Nazionale (PRIN) No. 2001024324_01302".

References

1. D. Savran *et al.*, Prog. Part. Nucl. Phys. **70**, 210 (2013).
2. I. Tanihata, H. Savajols, R. Kanungo, Prog. Part. Nucl. Phys. **68**, 215 (2013).
3. P. Adrich *et al.*, Phys. Rev. Lett. **95**, 132501 (2005).
4. O. Wieland *et al.*, Phys. Rev. Lett. **102**, 092502 (2009).
5. D.M. Rossi *et al.*, Phys. Rev. Lett. **111**, 242503 (2013).
6. J. Gibelin *et al.*, Phys. Rev. Lett. **101**, 212503 (2008).
7. A. Tamii *et al.*, Phys. Rev. Lett. **107**, 062502 (2011).
8. U. Kneissl, H.H. Pitz, A. Zilges, Prog. Part. Nucl. Phys. **37**, 349 (1996).
9. S. Goriely, Phys. Lett. B **436**, 10 (1998).
10. S. Goriely, E. Khan, M. Samyn, Nucl. Phys. A **739**, 331 (2004).
11. E. Litvinova *et al.*, Phys. Rev. C **79**, 054312 (2009).
12. B. Alex Brown, Phys. Rev. Lett. **85**, 5296 (2000).
13. R.J. Furnstahl, Nucl. Phys. A **706**, 85 (2002).
14. J. Piekarewicz *et al.*, Phys. Rev. C **85**, 041302 (2012).
15. P.-G. Reinhard, W. Nazarewicz, Phys. Rev. C **81**, 051303 (2010).
16. J. Piekarewicz, Phys. Rev. C **83**, 034319 (2011).
17. J. Piekarewicz, Phys. Rev. C **73**, 044325 (2006).
18. A. Klimkiewicz *et al.*, Phys. Rev. C **76**, 051603 (2007).
19. N. Tsoneva, H. Lenske, Phys. Rev. C **77**, 024321 (2008).
20. A. Carbone *et al.*, Phys. Rev. C **81**, 041301 (2010).
21. D. Vretenar *et al.*, Phys. Rev. C **85**, 044317 (2012).
22. J.M. Lattimer *et al.*, Annu. Rev. Nucl. Part. Sci. **62**, 485 (2012).
23. T. Hashimoto *et al.*, arXiv:1503.08321v1 [nucl-ex] (2015).
24. M.B. Tsang *et al.*, Phys. Rev. C **86**, 015803 (2012).
25. C.M. Tarbert *et al.*, Phys. Rev. Lett. **112**, 242502 (2014).
26. N. Paar *et al.*, Rep. Prog. Phys. **70**, 691 (2007).
27. I. Hamamoto, H. Sagawa, Phys. Rev. C **53**, R1492 (1996).
28. F. Catara *et al.*, Nucl. Phys. A **624**, 449 (1997).
29. E.G. Lanza *et al.*, Phys. Rev. C **79**, 054615 (2009).
30. E.G. Lanza *et al.*, Phys. Rev. C **84**, 064602 (2011).
31. T. Inakura *et al.*, Phys. Rev. C **84**, 021302 (2011).
32. E. Yüksel *et al.*, Nucl. Phys. A **877**, 35 (2012).
33. X. Roca-Maza *et al.*, Phys. Rev. C **85**, 024601 (2012).
34. J. Terasaki, J. Engel, Phys. Rev. C **74**, 044301 (2006).
35. K. Yoshida, N. Van Giai, Phys. Rev. C **78**, 064316 (2008).
36. M. Martini *et al.*, Phys. Rev. C **83**, 064309 (2011).
37. H. Hergert *et al.*, Phys. Rev. C **83**, 064317 (2011).
38. P. Papakonstantinou *et al.*, Phys. Lett. B **709**, 270 (2012).
39. D. Gambacurta *et al.*, Phys. Rev. C **84**, 034301 (2011).
40. M. Tohyama, T. Nakatsukasa, Phys. Rev. C **85**, 031302 (2012).
41. T. Hartmann *et al.*, Phys. Rev. Lett. **93**, 192501 (2004).
42. N. Tsoneva *et al.*, Nucl. Phys. A **731**, 273 (2004).
43. J. Liang *et al.*, Phys. Rev. C **75**, 054320 (2007).
44. D. Vretenar *et al.*, Nucl. Phys. A **692**, 496 (2001).
45. N. Paar *et al.*, Phys. Rev. C **67**, 034312 (2003).
46. N. Paar *et al.*, Phys. Rev. Lett. **103**, 032502 (2009).
47. D. Peña *et al.*, Phys. Rev. C **79**, 034311 (2009).
48. E. Litvinova *et al.*, Phys. Rev. C **78**, 014312 (2008).
49. E. Litvinova *et al.*, Phys. Rev. Lett. **105**, 022502 (2010).
50. G.R. Satchler, W.G. Love, Phys. Rep. **55**, 183 (1979).
51. G.R. Satchler, *Direct Nuclear Reactions* (Oxford University Press, 1983).
52. G. Bertsch, J. Horysowicz, H. McManus, W.G. Love, Nucl. Phys. A **284**, 399 (1977).
53. Dao T. Khoa, W. von Oertzen, Phys. Lett. B **342**, 6 (1995).
54. Dao T. Khoa *et al.*, Phys. Rev. C **56**, 954 (1997).
55. T.J. Deal, Nucl. Phys. A **217**, 210 (1973).
56. M.N. Harakeh, A.E.L. Dieperink, Phys. Rev. C **23**, 2329 (1981).
57. E.G. Lanza *et al.*, Phys. Rev. C , 054607 (2015).
58. P.D. Kunz, DWUCK4 code for DWBA at `http://spot.colorado.edu/ kunz/DWBA.html`.
59. T.D. Poelhekken *et al.*, Phys. Lett. B **278**, 423 (1992).
60. K. Govaert *et al.*, Phys. Rev. C **57**, 2229 (1998).
61. J. Endres *et al.*, Phys. Rev. C **85**, 064331 (2012).
62. V. Derya *et al.*, Phys. Lett. B **730**, 288 (2014).
63. V. Derya *et al.*, J. Phys. Conf. Ser. **366**, 012012 (2012).
64. J. Endres *et al.*, Phys. Rev. Lett. **105**, 212503 (2010).
65. J. Endres *et al.*, Phys. Rev. C **80**, 034302 (2009).
66. D. Savran *et al.*, Phys. Rev. Lett. **97**, 172502 (2006).
67. P. Decowski, H. Morsch, W. Benenson, Phys. Lett. B **101**, 147 (1981).
68. E.G. Lanza *et al.*, Phys. Rev. C **89**, 041601 (2014).
69. A. Bracco, F.C.L. Crespi, EPJ Web of Conferences **38**, 03001 (2012).
70. F.C.L. Crespi *et al.*, Phys. Rev. Lett. **113**, 012501 (2014).
71. L. Pellegri *et al.*, Phys. Lett. B **738**, 519 (2014).
72. M. Krzysiek *et al.*, Phys. Scr. **89**, 054016 (2014).
73. F.C.L. Crespi *et al.*, Phys. Rev. C **91**, 024323 (2015).
74. J.R. Beene *et al.*, Phys. Rev. C **39**, 1307 (1989).
75. J.R. Beene *et al.*, Phys. Rev. C **41**, 920 (1990).
76. J. Barrette *et al.*, Phys. Lett. B **209**, 182 (1988).
77. J.R. Beene *et al.*, Nucl. Phys. A **482**, 407 (1988).
78. D.J. Horen *et al.*, Phys. Rev. C **44**, 128 (1991).
79. A. Bracco *et al.*, Nucl. Phys. A **482**, 421c (1988).
80. S. Landowne *et al.*, Phys. Lett. B **90**, 389 (2014).
81. A.M. van der Berg *et al.*, Nucl. Phys. A **578**, 238 (1994).
82. J. Blomgren *et al.*, Nucl. Phys. A **578**, 239 (1994).
83. P. Heckman *et al.*, Phys. Lett. B **555**, 43 (2003).
84. C. Cabot *et al.*, *Conference Proceedings Of the XXIX Winter Meeting on Nuclear Physics in Bormio (Italy), Jan. 14–19, 1991.*
85. R. Liguori Neto *et al.*, Nucl. Phys. A **560**, 733 (1993).
86. R.L. Auble *et al.*, Phys. Rev. C **41**, 2620 (1990).
87. D. Mengoni *et al.*, Nucl. Instum. Methods Phys. Res. A **764**, 241 (2014).
88. S. Akkoyun *et al.*, Nucl. Instrum. Methods A **668**, 26 (2012).
89. A. Gadea *et al.*, Nucl. Instrum. Methods A **654**, 88 (2011).
90. S. Agostinelli *et al.*, Nucl. Instrum. Methods A **506**, 250 (2003).
91. E. Farnea *et al.*, Nucl. Instrum. Methods A **621**, 331 (2010).
92. N. Ryezayeva *et al.*, Phys. Rev. Lett. **89**, 272502 (2002).
93. T. Shizuma *et al.*, Phys. Rev. C **78**, 061303 (2008).
94. L. Pellegri *et al.*, Phys. Rev. C **92**, 014330 (2015).
95. RF Casten, *Nuclear Structure from a Simple Perspective* (Oxford University Press, Oxford 1990).
96. I.J. Thompson, Comput. Phys. Rep. **7**, 167 (1988).
97. `http://www.fresco.org.uk/index.htm`.
98. T.P. Sjoreen *et al.*, Phys. Rev. C **29**, 1370 (1984).
99. J. Heisenberg *et al.*, Phys. Rev. C **29**, 97 (1984).
100. N. Tsoneva, H. Lenske, Phys. Lett. B **695**, 174 (2011).
101. R. Schwengner *et al.*, Phys. Rev. C **78**, 064314 (2008).
102. C. Iwamoto *et al.*, Phys. Rev. Lett. **108**, 262501 (2012).
103. A. Krugmann *et al.*, EPJ Web of Conferences **66**, 02060 (2014).

Angela Bracco is a full Professor at the University of Milano and she is associated to INFN. Her research experience is in nuclear structure and she obtained relevant results on the giant dipole resonance at zero and finite temperature. She was involved in the realization of complex detection system for gamma-ray built in European collaboration (EUROBALL, RISING and AGATA). In 2005–2011 she chaired the Nuclear Physics board of INFN and presently she is the chair of NuPECC (the European expert committee for Nuclear science).

Edoardo G. Lanza is a theoretical nuclear physicist. He is a senior researcher of the Italian Institute for Nuclear Physics (INFN). He graduated at Catania University and received the doctoral degree at the Heidelberg University. He has been awarded a senior Marie Curie Fellowship in 1989. He has been working in heavy-ion physics and in quantum chaos. Recently his main interest has been devoted to collective states in nuclei with neutron excess with a particular attention to the so-called pygmy dipole resonance.

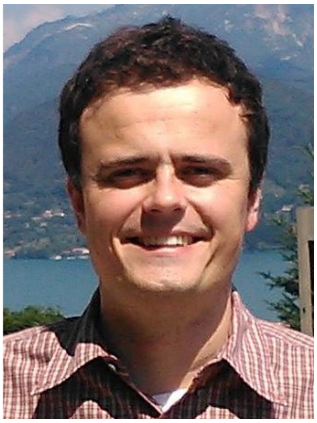

Fabio Crespi received his doctoral degree from the Università degli Studi di Milano in 2008. His research activity focuses on the experimental study via gamma spectroscopy of nuclear properties, in particular collective excitations, at extreme conditions of temperature, angular momentum and isospin. He has been strongly involved in experiments using stable and radioactive beams at several facilities worldwide (*e.g.*, LNL-INFN, GANIL, GSI, RIKEN). He had responsabilities in experiments made with the AGATA array, constructed as a large European collaboration. An important part of his activity is devoted to R&D for detectors.